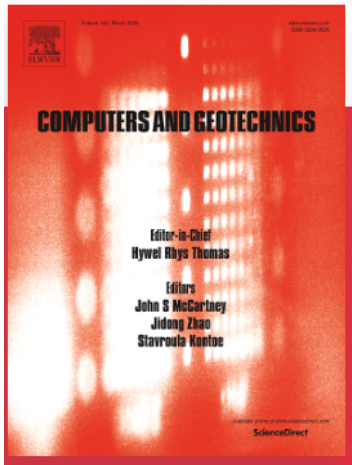

Discrete element method analysis of non-linear stiffness for granular media

Graphical Abstract

Discrete element method analysis of non-linear stiffness for granular media

H.C. Nguyen

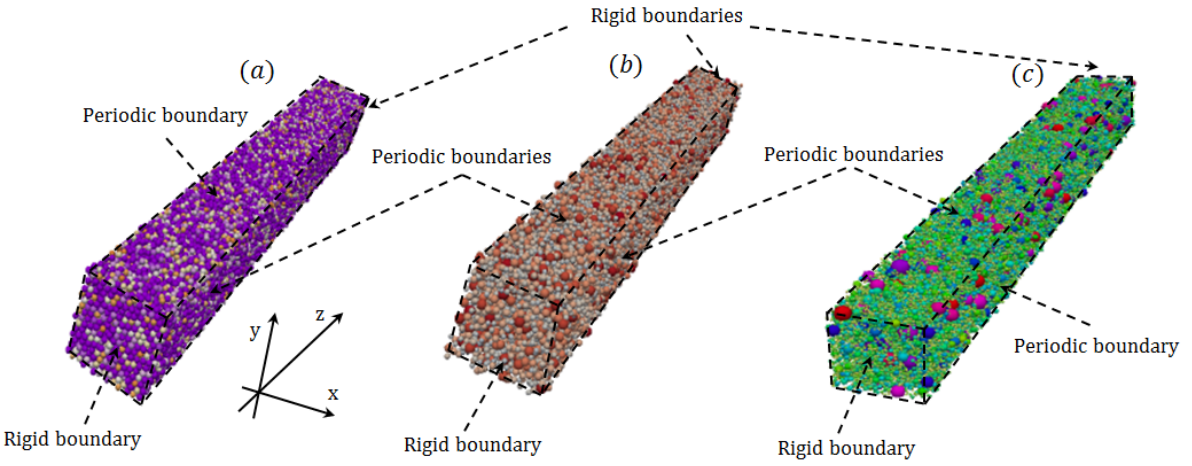

Highlights

Discrete element method analysis of non-linear stiffness for granular media

H.C. Nguyen

- The modified formulation of hyperbolic relation based on the DEM data is generated to capture stiffness degradation, which can take the various types of an S-shaped curve due to the initial mean effective stress and the sample density.
- DEM results reveal that inclusion of the coordination number in both forms of the void ratio function serve a better role in the removal of void ratio effects on the stiffness degradation curve.
- Several DEM simulations were performed to assess effects of the coefficient of uniformity (C_u) on the non-linear behaviour of granular materials, arriving at some key observations that: (i) a higher amount of work should be input for samples with coarse particles to attain a particular strain level; and (ii) more energy dissipation is observed for samples with a lower C_u value.
- The framework of kinematic modified yielding points proposed by Jardine (1992) that identifies three main zones (i.e. linear elastic behaviour, non-linear elastic behaviour and elasto-plastic behaviour) provides a benchmark for the gap between the dynamic stiffness and the static stiffness to be studied in an effective manner.
- A key observation is that the dynamic shear stiffness tends to increase to a peak value before experiencing of a decrease in magnitude.

Discrete element method analysis of non-linear stiffness for granular media

H.C. Nguyen[a,b]

[a]Department of Civil Engineering and Industrial Design, University of Liverpool, Liverpool, UK
[b]Former PhD student, Department of Civil and Environmental Engineering, Imperial College London, Skempton Building, London, UK

ARTICLE INFO

Keywords:
Non-linear stiffness
DEM simulations
The hyperbolic form
Energy dissipation
The coefficient of uniformity

ABSTRACT

This contribution considers the nonlinearity of stiffness in granular materials using 3D DEM simulations, with a primary focus being placed on three issues. First, it assesses stress-dependent stiffness and density-dependent stiffness based on DEM simulations of monotonic triaxial tests. The modified formulation of hyperbolic relation based on the DEM data is generated to capture stiffness degradation, which can take the various types of an S-shaped curve due to the initial mean effective stress and the sample density. The use of various void ratio correction functions is made to remove the effect of density on the stiffness curve. DEM results reveal that inclusion of the coordination number in both forms of the void ratio function serve a better role in unifying the stiffness dataset from samples with different densities. Second, the framework of kinematic modified yielding points proposed by Jardine (1992) that identifies three main zones (i.e. linear elastic behaviour, non-linear elastic behaviour and elasto-plastic behaviour) provides a benchmark for the gap between the dynamic stiffness and the static stiffness to be studied in an effective manner. A key observation is that the dynamic shear stiffness tends to increase to a peak value before experiencing of a decrease in magnitude. Third, the investigation into the nature of energy dissipation during triaxial shearing tests is made. Several DEM simulations were performed to assess effects of the coefficient of uniformity (C_u) on the non-linear behaviour of granular materials, arriving at some key observations that: (i) a higher amount of work should be input for samples with coarse particles to attain a particular strain level; and (ii) more energy dissipation is observed for samples with a lower C_u value.

1. Introduction

Several geotechnical engineering problems require information on the non-linear evolution of stiffness with strain. Different types of infrastructure (i.e. retaining walls, foundations and tunnels) impose a deformation with a different range of strains. It is well-known that the behaviour of granular materials is highly non-linear (Atkinson, 2000; Atkinson et al., 1990). In particular, the stiffness has a non-linear dependency on the strain level. Use of normalised stiffness and consideration of the variation of this normalised stiffness with strain allow the nonlinearity of stiffness to be investigated (Oztoprak and Bolton, 2013; Houlsby and Wroth, 1991). The extent to which the shear stiffness decays with shear deformation depends on the stress state, sample density, stress paths (Atkinson et al., 1990; Oztoprak and Bolton, 2013). At small-strain levels (Clayton, 2011), the elastic stiffness remains constant at its maximum value, followed by a drop in stiffness as the strain level increases. Experimental data indicate that the shear stiffness decays rapidly as the plastic strains become more significant than the elastic strains (Jardine et al., 1984, 1986). It is useful to express the stiffness degradation curve in terms of hyperbolic expressions (Darendeli, 2001; Hardin and Drnevich,

ORCID(s): 0000-0001-6599-2790 (H.C. Nguyen)

1972; Fahey and Carter, 1993; Menq, 2003; Oztoprak and Bolton, 2013) with the use of a few parameters, allowing the secant stiffness at a certain strain level to be predicted.

It is well-known that the shear modulus is strain dependent. At a given strain level, this parameter can be measured using different types of test, with the appropriate technique. The extent to which these techniques will give the different stiffness values remains poorly understood. In the triaxial test, for example, the bender elements and the stress:deformation data from both monotonic triaxial tests have been widely used to measure the shear stiffness. At small-strain levels, bender elements provide a useful means to measure soil stiffness in the laboratory testing (Viggiani and Atkinson, 1995; Bellotti et al., 1996; Jovičić and Coop, 1998; Greening and Nash, 2004; Clayton, 2011). At a higher strain level, the shear stiffness is widely inferred from the stress-deformation data from local gauges and conventional soil testing (Atkinson, 2000). Herein we use both the shear wave velocity and the stress-strain relationship to estimate the shear modulus, allowing the gap between statically determined static and dynamic stiffness to be investigated. For convenience in making comparisons between these methods, the term "dynamic stiffness" is used to mean stiffness measured from stress wave propagation data and the term "static stiffness" is used to mean the stiffness measured from the stress-strain relationship. Due to the fact that these methods to measure stiffness are based on different mechanisms, it is worth exploring difference between the stiffnesses measured from each of these approaches in the triaxial apparatus. The relevant questions are raised as follows:

1. Over which strain range does the ratio of the dynamically measured stiffness to the statically calculated stiffness remain unchanged?

2. How does dynamic stiffness evolve with strain level?

In order to address the above questions, both DEM simulations of monotonic triaxial tests and DEM simulations of planar wave propagation were carried out on assemblies of monodisperse size, with two different densities. The samples were sheared along conventional triaxial stress paths in which both lateral stress components were kept constant and the vertical stress increased. At discrete strain levels, the shear modulus was calculated using two methods, allowing differences between the static and dynamic measures of stiffness to be investigated. The yielding points proposed by Jardine (1992) provides useful strain thresholds at which these comparisons are made. There is also a discussion and observation of the evolution of dynamic stiffness with increasing strain levels.

It is widely recognised that the numerical modelling using the discrete element method (DEM) proposed by Cundall and Strack (1979) provides a powerful means to further fundamental understanding of the grain-scale mechanisms underlying observations from macro-scale laboratory testing. Over recent decades, the use of DEM simulations in geomechanics studies has continued to grow, as noted by O'Sullivan (2011a). DEM models have the following characteristics: (i) they can capture the highly complex behaviour of sand; (ii) using particulates in the simulations does not require the continuum assumptions to be adopted; and (iii) they can provide micro-scale parameters for fundamen-

tal research into the grain-scale mechanisms. High-performance computing (HPC) facilities allow a large number of particles to be considered in the analysis for the study on stiffness using DEM simulations (O'Sullivan, 2011b). DEM simulations of triaxial tests can be used to measure the stiffness of granular materials while also providing micro-scale data to further a fundamental understanding of the grain-scale mechanisms. As outlined by O'Sullivan (2011a), while the use of this discrete numerical approach to study soil stiffness has grown, a limited number of studies using micromechanics-based tools have looked at the small-strain stiffness under anisotropic stress conditions and the stiffness degradation curve.

In addition, DEM data allow the dissipation of both micro-scale and macro-scale energy during triaxial shearing to be investigated. Building on the contribution of Hanley et al. (2018), the individual components of energy are analysed using the DEM simulations of the triaxial test which are sheared along different stress paths. As noted by Hanley et al. (2018), a key element of the development of a model is the consideration of energy conservation. The Cam-Clay model, for instance, is based on the assumption that much of plastic dissipation is due to friction. This provides motivation for a study that compare the work input per unit volume with the frictional dissipation associated with sliding friction during shearing, with an expectation that both energies should be almost equal (Hanley et al., 2018). Although the evolution of each energy component (i.e. translational and rotational energy) is mainly dependent upon the path along which the sample is sheared, this issue has not previously been given detailed consideration. We re-examine the assumption that frictional dissipation and boundary are equal in magnitude. Although particle crushing is also attributed to energy dissipation (Bolton et al., 2008), this source of energy dissipation is ignored in this study.

It is widely accepted that the particle shape (Houlsby, 2009) has a significant effect on the granular material. Cho et al. (2007) experimentally confirmed that increasing particle irregularity results in a reduction in the shear stiffness. Liu and Yang (2018) stated that the small-strain stiffness reduces when the sand grains become more rounded. It is reported by Xiao et al. (2019) that a rise in the combined overall regularity leads to a significant drop in the compressive strength and the secant shear modulus. However, herein DEM simulations of triaxial tests (O'Sullivan, 2011b; Nguyen et al., 2017, 2018; Nguyen and O'Sullivan, 2019; Nguyen, 2020, 2021a) were performed on the spherical particles to further the fundamental understanding of the non-linear stiffness of soil which is a long-standing topic of interest in geomechanics, with the degree of nonlinearity being influenced by many factors, including the stress path, the sample density and the particle size distribution. Both the macro-scale and the micro-scale data gathered from the true-triaxial DEM simulations allow the non-linearity of stiffness and the interactions at the particle scale to be further understood. Although the sample size and the representative element volume (REV) has a certain effect on both micro and macro-scale responses (Huang et al., 2014; Ciantia et al., 2019; Adesina et al., 2022), herein the combination of both periodic and rigid boundaries is appropriate for measurements of both static and dynamic stiffnesses. The coordination number provides a complementary insight to further understand the macro-scale response of granular materials. The static

stiffness and the dynamic stiffness are measured at a certain strain level, allowing the degree of nonlinearity of stiffness to be studied. Comparison with the static stiffness is made to assess the gap between the dynamic and static stiffness as the shear strain increases. The postulation that these discrepancies between two different measurements of the shear stiffness dependents on the interpretative techniques is achieved, in which the frequency domain gives the dynamic stiffness closer to the static stiffness. The framework of kinematic modified yielding points proposed by Jardine (1992) that identifies three main zones (i.e. linear elastic behaviour, non-linear elastic behaviour and elastoplastic behaviour) provides a benchmark for the nature of non-linear stiffness to be studied effectively. The mathematical formulations used to capture the non-linear stiffness degradation curves are examined in detail, the hyperbolic form is found to closely capture the reductions in shear stiffness with increasing strain. Following prior experimental contributions (Liu and Yang, 2018; Liu et al., 2016; Wichtmann and Triantafyllidis, 2009), several DEM simulations on samples with various coefficients of uniformity (C_u) that vary from 2 to 6 were carried out, leading to some key observations that: (i) samples with lower values of C_u have higher stiffness at small-strain levels; (ii) a higher amount of work should be input for samples with coarse particles to attain a particular strain level; and (iii) more energy dissipation is observed for samples with a lower C_u value.

2. Background to the non-linearity of stiffness

It is widely accepted that much of the focus of studies on the shear modulus is placed on two main aspects. The first is the form of the void ratio function, while the second is principally concerned with the changes in the parameters that describe the stiffness:strain relationship (i.e. $G_{sec} = C_p(\gamma)F(e)p'^{n(\gamma)}$). This chapter considers the void ratio correction function over a wider range of strain levels (i.e. from the very small strain, $\epsilon_a < 0.001\%$ to the medium strain level, $\epsilon_a < 0.5\%$). Apart from investigations into the function F(e), both $C_p(\gamma)$ and $n(\gamma)$ are reexamined using DEM data. Experimental studies (Oztoprak and Bolton, 2013) indicate that $C_p(\gamma)$ reduces with increasing shear strain and this trend is in contrast with the variation in $n(\gamma)$ (i.e. $n(\gamma)$ varies from 0.5 to 1.0 as γ increases). These findings are revisited by using data obtained from true-triaxial DEM simulations with stress-induced anisotropy. In order to assess the variations in C_p and m with γ, a void ratio function of the form $F(e) = (1 + e)^{-3}$ was adopted in the work of Oztoprak and Bolton (2013). Plot of $G_{sec}/F(e)p_a$ against p'/p_a give the value of both C_p and n at a given strain level. It is important to recognise that the void ratio correction function selected changes the value of both C_p and m (Nguyen, 2020). This provides the motivation to use two types of the void ratio correction function to estimate C_p and m as discussed by Nguyen (2020).

Much prior study research has shown that the nonlinearity of stiffness is hyperbolic in shape, so various forms of hyperbola have been adopted to describe the variation of stiffness with strain. In geotechnical design, a simple formulation that can capture the stiffness curve is useful. Hardin and Drnevich (1972) related stiffness at a given strain

level to the maximum stiffness by the following formulation

$$G_0 = G_{sec}\left(1 + \frac{\gamma}{\gamma_r}\right) \tag{1}$$

where G_0 is the maximum shear modulus, G_{sec} is the secant shear modulus at a given strain level, γ is the shear strain, and γ_r is the reference shear strain measured at τ_{max}/G_0. Central to this formulation is quantifying the value of the reference strain, γ_r. Instead of using shear strain levels in the normalised formulation, Darendeli (2001) included shear stress in the hyperbolic formulation such that

$$G_0 = G_{sec}\left(1 - m\left[\frac{\tau}{\tau_{max}}\right]^n\right) \tag{2}$$

where m and n are two empirical parameters, τ is the shear stress at a certain level of γ. It is also recognized that the measurement of τ_{max} is also the main challenge in this mathematical formulation.

Darendeli (2001) used the formulation proposed by Hardin and Drnevich (1972), but took the reference strain to be at $G_{sec}/G_0 = 0.5$ and proposed a curvature parameter that accounts for the nonlinearity of stiffness as described in the following expression:

$$G_0 = G_{sec}\left(1 - \gamma\left[\frac{\gamma}{\gamma_r}\right]^m\right) \tag{3}$$

Following the earlier contributions, Oztoprak and Bolton (2013) introduced a hyperbolic relationship to capture stiffness degradation that can take the form of an S-shaped curve. This newly modified formulation is based on a large set of test data on various sands. The best-fit functional relationship is similar to the expression proposed by Darendeli (2001), but considers the difference between the given shear strain and the elastic strain threshold, γ_e as shown in the following expression:

$$G_0 = G_{sec}\left(1 + \left[\frac{\gamma - \gamma_e}{\gamma_r}\right]^m\right) \tag{4}$$

In the study of Darendeli (2001), the stiffness at a strain level of 0.0001% is considered to be the maximum stiffness (i.e. G_0 at $\gamma = 0.0001\%$). The elastic strain threshold can be mapped using the schematic of multiple yield surfaces proposed by Jardine (1992). In particular, the location of yield point Y_1 is the value of γ_e. Due to the path-dependent and density-dependent nature of stiffness, using these two strain levels as bounds to bracket the stiffness degradation region provides some advantages. Adjustment of the parameters in Equation 4 (i.e. γ_e and γ_r) is required to accurately capture the stiffness degradation region.

In addition, the curvature parameter, m is dependent on the sample density (Darendeli, 2001; Menq, 2003; Oztoprak and Bolton, 2013). A brief overview of studies on this parameter is given here. A curvature parameter of 0.92 was adopted for undisturbed sandy and gravelly soils in the study of Darendeli (2001). Using the results of tests on Toyoura sand, Menq (2003) concluded that the curvature parameter is likely to be independent of the confining pressure; however, for dry sandy and gravelly soil m values can be estimated as $m = 0.86 + 0.1log(p'/p_a)$. Oztoprak and Bolton (2013) reported that the value of m is independent upon the mean effective stress but changes with soil type and state (i.e. mean grain size, uniformity coefficient and void ratio). The values of m vary from 0.75 to 1.0 when the whole database is considered. Oztoprak and Bolton (2013) found that there is a correlation between m and the coefficient of uniformity, C_u, as given by the following relationship:

$$m = C_u^{-0.075} \tag{5}$$

While the particle size distribution is a major influence on the stress-deformation relationships in granular materials, very little investigation into the fundamental origin of this sensitivity has been made in the literature. Using DEM simulations with linear PSDs (Shire, 2014; Shire and O'Sullivan, 2016; Otsubo et al., 2017; Liu et al., 2021) and systematically varying the C_u value allows the effects of PSDs on the stiffness degradation curve to be explored. Herein, the focus is placed on altering the stiffness degradation curve as the particle size distributions are varied from uniform to broadly-graded samples. Two bounds expressed as hyperbolic formulations are then proposed. In addition, the suggestion of Oztoprak and Bolton (2013) that the curvature parameter is a function of C_u (i.e. $m = C_u^{-0.075}$) is reexamined using DEM data generated here.

Hanley et al. (2018) reported that the boundary work is almost equal to the frictional dissipation, regardless of the sample density. DEM simulations of samples with PSDs allow the gap between the energy dissipation and the input work to be revisited. Although changes in PSDs result in variations in plastic dilatancy at a given strain level, investigations into this change have not been addressed in the literature. The DEM simulations of triaxial compression tests on samples with differing PSDs allows this issue to be explored. The dependency of contacts on the material PSD is then studied, focusing on the change in this dissipation with axial strain. Two components of the boundary work, i.e. volumetric and distortional work, are computed to assess the effects of the material PSD on the evolution in these energies with increasing shear strain. Assessments of contact distributions due to variations in grain sizes are made, with a focus on the sensitivity of the preferential orientations to the PSD.

Table 1
DEM simulation parameters.

Parameter	Notation	Value	Unit
Particle size	d_p	2.54	mm
Particle density	ρ_p	2230	kg/m^3
Interparticle friction	μ_p	0.35	NA
Particle shear modulus	G_p	25×10^9	Pa
Particle Poisson's ratio	ν_p	0.2	NA
Transmitter frequency	f	20	kHz
Amplitude of sinusoidal motion	A	2.5	nm

3. DEM simulations

Simulations of triaxial compression tests were conducted on samples with two different densities using a modified version of the granular LAMMPS code (Plimpton, 1995), with a simplified Hertz-Mindlin contact model. Each sample was created from an initial cloud of 34, 986 non-contacting monodisperse spherical particles. The samples were enclosed in the vertical direction by two rigid, planar, horizontal boundaries; periodic boundaries were used in the lateral direction as illustrated in Figure 1. To vary density, two values of inter-friction were used as the sample was isotropically compressed to an initial mean effective stress of $p'_0 = 1kPa$; the randomly monodisperse dense sample (RMD) was created using $\mu_p = 0$, while $\mu_p = 0.15$ was used to generate the randomly monodisperse loose sample (RML). These two samples were isotropically compressed to three different mean effective confining pressures, $p'_0 = 50kPa$, $p'_0 = 300kPa$ and $p'_0 = 1000kPa$ using a servo-control algorithm (Thornton and Antony, 1998), with the use of the same value of $\mu_p = 0.35$ for both samples in this process. It should be noted that periodic boundaries were used to control the lateral stresses, σ_x and σ_y, while the vertical stress was controlled using the rigid wall boundaries σ_z. Once a desired value of the mean effective pressure was achieved, DEM simulations of triaxial shearing tests were performed, along the path in which constant $\sigma_x = \sigma_y$ and increasing σ_z are satisfied. At a given stress state or strain level, the secant shear modulus, G_{sec} such that $G_{sec} = \frac{\Delta q}{3\Delta\epsilon_s}$. The deviator stress is taken as $\Delta q = \sigma_z - 0.5(\sigma_x + \sigma_y)$; and the deviator strain, ϵ_s was calculated as $\epsilon_s = 2/3(\epsilon_z - \epsilon_x)$ where ϵ_z and ϵ_x are the major and minor normal strains.

Apart from calculation of static stiffness, DEM simulations were performed to estimate the dynamic stiffness based on the shear wave velocity. At a stress level, shear waves were then generated by applying a single-period sine motion to one rigid wall in a particular direction and the opposite wall was used to analyse received signals. For example, exciting a rigid wall, for instance in the $x-$ direction aims to deduce wave propagation in the horizontal plane as illustrated in Figure 1. The speed of wave transmitted, V_{zx} can be estimated by considering changes in the shear stress in the exciting direction of both rigid walls with time. The elastic behaviour of granular systems allows calculating the corresponding shear modulus, G_{zx} as shown in Figure 1.

Following the work of Shire (2014) and and the experimental study (Liu and Yang, 2018), several DEM simulations

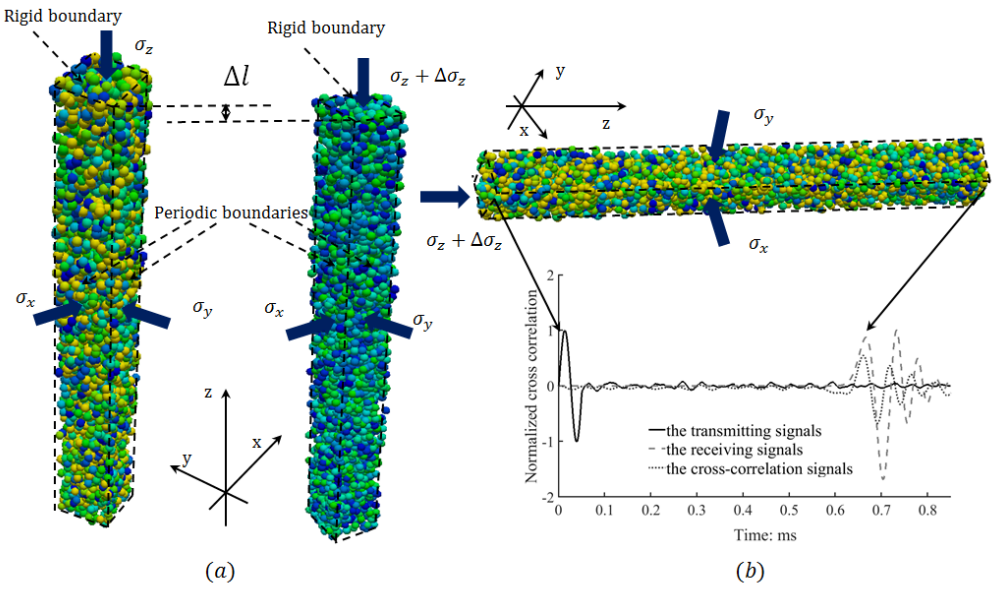

Figure 1: Illustrations of measurements of shear stiffness: (a) the static method using DEM simulations of triaxial probes; and (b) the dynamic method using DEM simulations of shear wave propagation.

were performed on samples of linear PSDs with varying C_u values from from as low as 2 to as high as 6. In particular, samples with linearly graded PSDs which have $C_u = 2, 3, 5, 6$ were generated, with the minimum particle diameter being 1 *mm* in all cases (Figure 2). The size of samples is the same as that of monodisperse samples and a simplified Hertz-Mindlin contact model was adopted in all simulations, having mixed periodic and rigid wall boundaries as illustrated in Figure 1 ($d_{min} = 1mm$, $\rho_p = 2230kg/m3$, interparticle friction coefficient $\mu_p = 0.35$, $G_p = 25GPa$ and particle Poison's ratio $\nu_p = 0.2$). Starting from an initial cloud of non contacting particles the samples were isotropically compressed to 1 kPa using three different inter-particle friction values (i.e. $\mu_p = 0.0, \mu_p = 0.1$ and $\mu_p = 0.2$), so as to generate samples with different values of density. The terms "dense", "medium" and "loose" were then adopted respectively in line with Shire (2014). Once a stable condition of $p'_0 = 1kPa$ was achieved, all samples were then compressed to isotropic confining pressures of $p'_0 = 100kPa$, $p'_0 = 300kPa$ and $p'_0 = 1000kPa$ using the same value of $\mu_p = 0.35$. At each initial mean effective stress, these samples were sheared along the stress path that both the σ_x and the σ_y were maintained constant while the σ_z was increased.

4. DEM anlysis

DEM results obtained using the modified LAMMPS code were validated by calculating the the exponential value of n in the relationship $G_0 \propto p'^n$. It is widely known that a power-law relationship has been widely considered to describe the relationship between the dynamic stiffness and the confining pressure. Based on linear regression analysis of the data plotted in the logarithmic scale, the power values are 0.353 for the RMD sample and 0.341 for the RML sample as

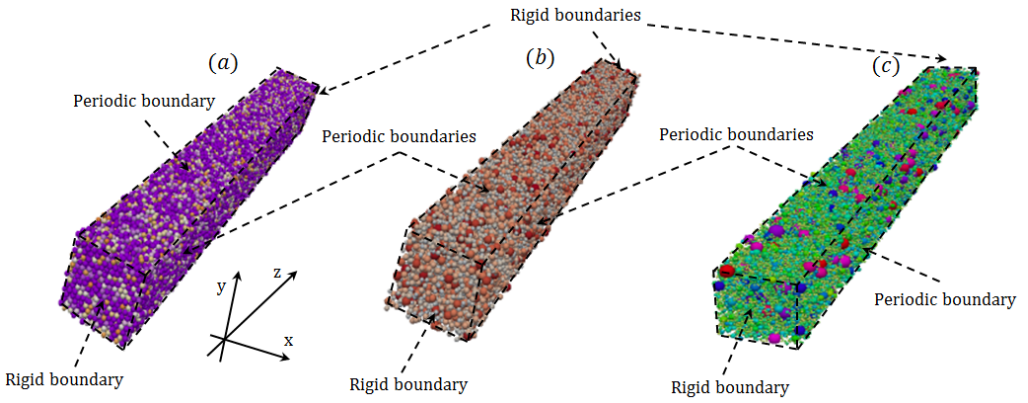

Figure 2: Samples with linear PSDs with the same size as that of monodisperse samples: (a) $C_u = 2$; (b) $C_u = 5$; and (c) $C_u = 6$.

shown in Figure 3. These power values agree well with the Hertzian contact theory and experimental values on glass bead ballotini with both smooth and rough surfaces Otsubo (2016).

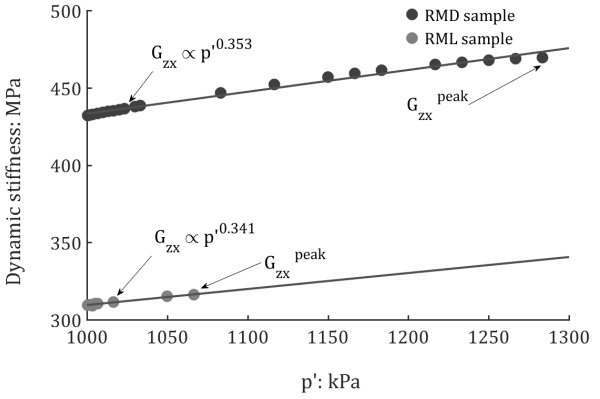

Figure 3: The power-law relationship between G_{Vs} and p' when samples were sheared at $p'_0 = 1000kPa$.

4.1. Overall responses

Using the deviator stress, q_{crit} and mean effective stress, p_{crit} at failure, the critical state angle of shearing resistance for the triaxial compression test is inferred from the following relationship:

$$M = \frac{6sin\phi_{crit}}{3 - sin\phi_{crit}} = \frac{q_{crit}}{p_{crit}} \tag{6}$$

where ϕ_{crit} is stress ratio, η dependent. Similar equation is adopted to calculate the friction angle at the peak strength; however, the use of both q and p' at the peak strength was made to determine ϕ_{peak}. Using DEM data from the triaxial compression test, the calculated friction angle at peaks and critical state are $\phi_{peak} = 23.98^o$ and $\phi_{cri} = 17.39^o$

respectively.

The overall response including the evolution of stress ratio and volumetric strain with axial strain are shown in Figure 4, enabling the variation in secant stiffness with the shear strain to be studied. It is numerically stated by Huang et al. (2014) and Adesina et al. (2022) that the size of sample should be large enough to avoid fluctuations observed in the stress-strain responses. It is shown in the Figure 4 that there is no fluctuations observed in the responses, allowing the stiffness degradation curve to be captured in a accurate manner. It is reasonable to expect that smaller system sizes are conducted to attain a REV samples where all periodic boundaries are used to avoid the disturbance occurred between rigid wall boundaries and the particles, and more details of the effect of the REV size on the macro-scale response can be found in the very recent contribution by Adesina et al. (2022). To analyze the pattern of stiffness degradation with strain, in which the secant stiffness was determined from the deviatoric stress and the deviatoric shear strain (i.e. $E_{sec} = q/3\epsilon_s$).

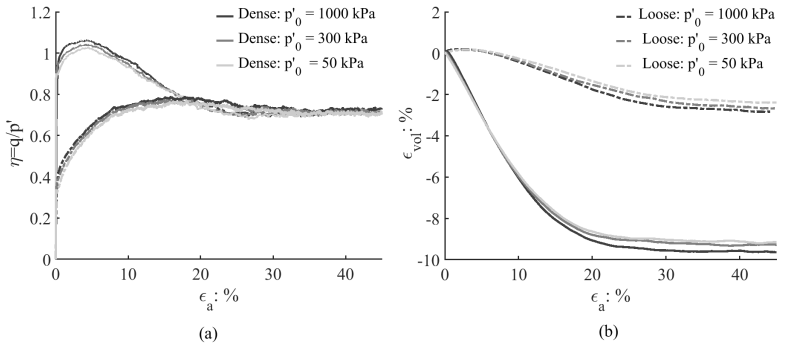

Figure 4: Overall responses of monodisperse sample.

4.2. Stiffness degradation of the monodisperse sample

E_{sec} and G_{sec} were computed from the load: deformation data for the two monodisperse samples. As is shown in Figure 5, E_{sec} and G_{sec} depend upon the confining pressure and the sample density; the randomly monodisperse dense sample has higher values of E_{sec} and G_{sec} than the randomly monodisperse loose sample. Normalisations of E_{sec} by E_0 and G_{sec} by G_0 were made to enable direct comparison of the degradation of stiffness with strain. Figure 6 shows reductions in moduli which are of importance in geotechnical designs. As described above, the use of hyperbolic forms to capture the shape of the degradation of stiffness with strain, i.e. the stiffness degradation curve, are widely adopted, serving as a useful means to predict stiffness values for use in engineering design with the use of only a few parameters.

Building the earlier contribution of Oztoprak and Bolton (2013), the hyperbolic form of $G_0 = G_{sec}\left(1 + \left[\frac{\gamma-\gamma_e}{\gamma_r}\right]^m\right)$ was applied to fit the secant shear modulus degradation data generated here. The analysis focussed on the variation in G_{sec}/G_0 with γ, taking γ_e to be the shear strain at the yield Y_1 and the reference strain, γ_r was taken at $G_{sec}/G_0 = 0.5$.

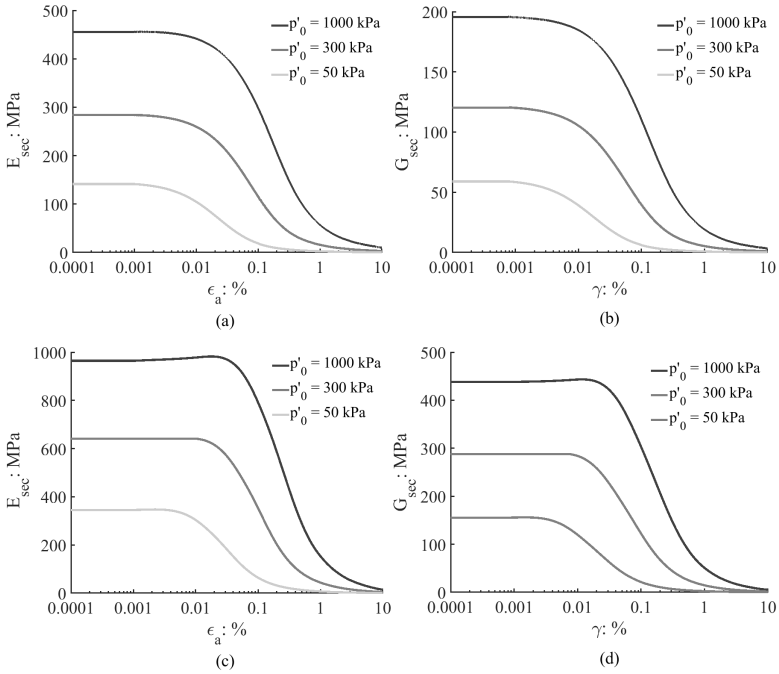

Figure 5: Stiffness degradation curves: (a) E_{sec}: the RML sample; (b) G_{sec}: the RML sample; (c) E_{sec}: the RMD sample; (d) G_{sec}: the RMD sample.

Table 2
Variations in the elastic threshold strain and the reference shear strain with the effective confining pressure and the sample density.

$p'_0 : kPa$	γ_e : % RML	γ_e : % RMD	γ_{vol} : % RML	γ_{vol} : % RMD
50 kPa	0.00081	0.00223	0.01738	0.02333
300 kPa	0.00079	0.00743	0.05456	0.07906
1000 kPa	0.00080	0.01182	0.12249	0.17949

The curvature parameter m was adjusted to closely capture the reduction in G_{sec}/G_0. The scheme to map multiple yield surfaces proposed by Jardine (1992) was used to identify the elastic threshold strain, γ_e. The summary data on Table 2 show that the elastic threshold strain increases with the effective confining stress for the dense sample; however, for the loose sample, this strain level likely remains unchanged when the initial shearing pressure varies from $p'_0 = 50kPa$ to $p'_0 = 1000kPa$.

The values for the curvature parameter obtained for the DEM simulation data are 1.1 for the RML samples and 1.2 for the RMD samples; these values of 1.1 and 1.2 are higher than those derived from Darendeli (2001) (i.e. $m = 0.92$) and Oztoprak and Bolton (2013) (i.e. $m = 0.82$). The stiffness degradation data are compared with data obtained from the hyperbolic equation in Figure 7 for the RMD and RML samples, respectively. In particular, the curvature value of $m = 1.1$ captures the stiffness reduction of the random loose sample very well, while the value of the curvature

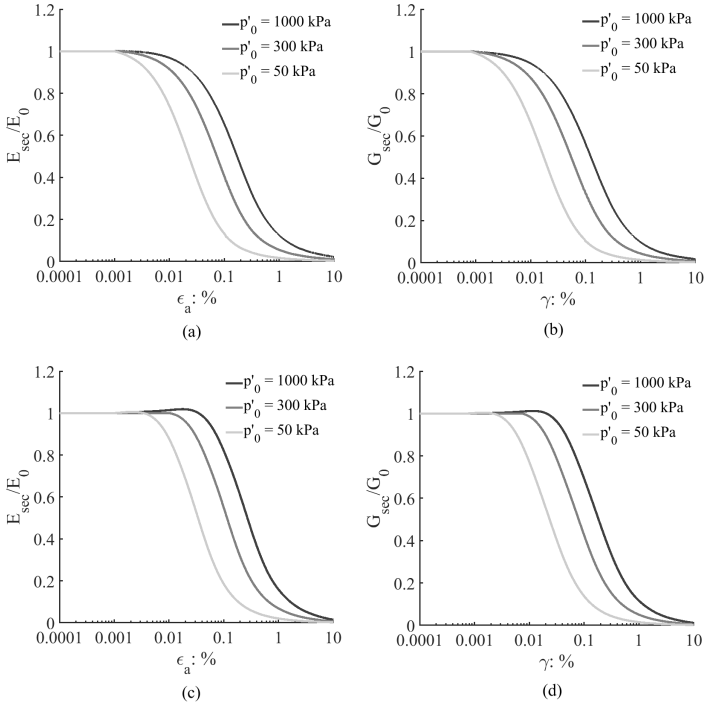

Figure 6: Normalised stiffness degradation curves: (a) E_{sec}/E_0: the RML sample; (b) G_{sec}/G_0: the RML sample; (c) E_{sec}/E_0: the RMD sample; (d) G_{sec}/G_0: the RMD sample.

parameter that best describes the variation in stiffness with strain for the dense sample is slightly higher than those of the loose sample. Interestingly, the most suitable curvature parameter value remains unchanged for the three different initial confining pressures; even both the elastic and reference strain are stress-dependent.

These observations confirm the prior findings (Menq, 2003) that m is likely to be independent of the confining pressure. Note that both elastic strain threshold, γ_e and the reference strain, γ_r are dependent on the confining pressure. Therefore, hyperbolic expressions can be used to obtain upper and lower bounds that describe a secant shear modulus degradation curve that result from shearing the sample at different initial confining pressures as shown in Figure 6. To address this issue, some modifications can be made using the hyperbolic form of $G_0 = G_{sec}\left(1 + \left[\frac{\gamma-\gamma_e}{\gamma_r}\right]^n\right)$, with a focus on the choice of both γ_e and γ_r.

It is noted that the role of void ratio correction function in eliminating the effect of sample density on small-strain stiffness, an extension to the removal of the effect of the void ratio on the shear modulus over a wider range of strain levels from small to large-scale is considered in this study. Both types of void ratio correction expression which are expressed in the forms of $F(e) = \frac{(B+1)^2}{1+e}$ and $F(e) = e^{-\lambda}$ were considered herein, with the inclusion of micro-scale parameters. According to Nguyen (2020), the use of the conventional form of the void ratio corrections does not resolve the gap of the normalised shear stiffness $G_{sec}/F(e)$ of two different initial densities. Therefore, the coordination number, N_c which is easily extracted from DEM simulations was made in the void ratio forms. It is noted

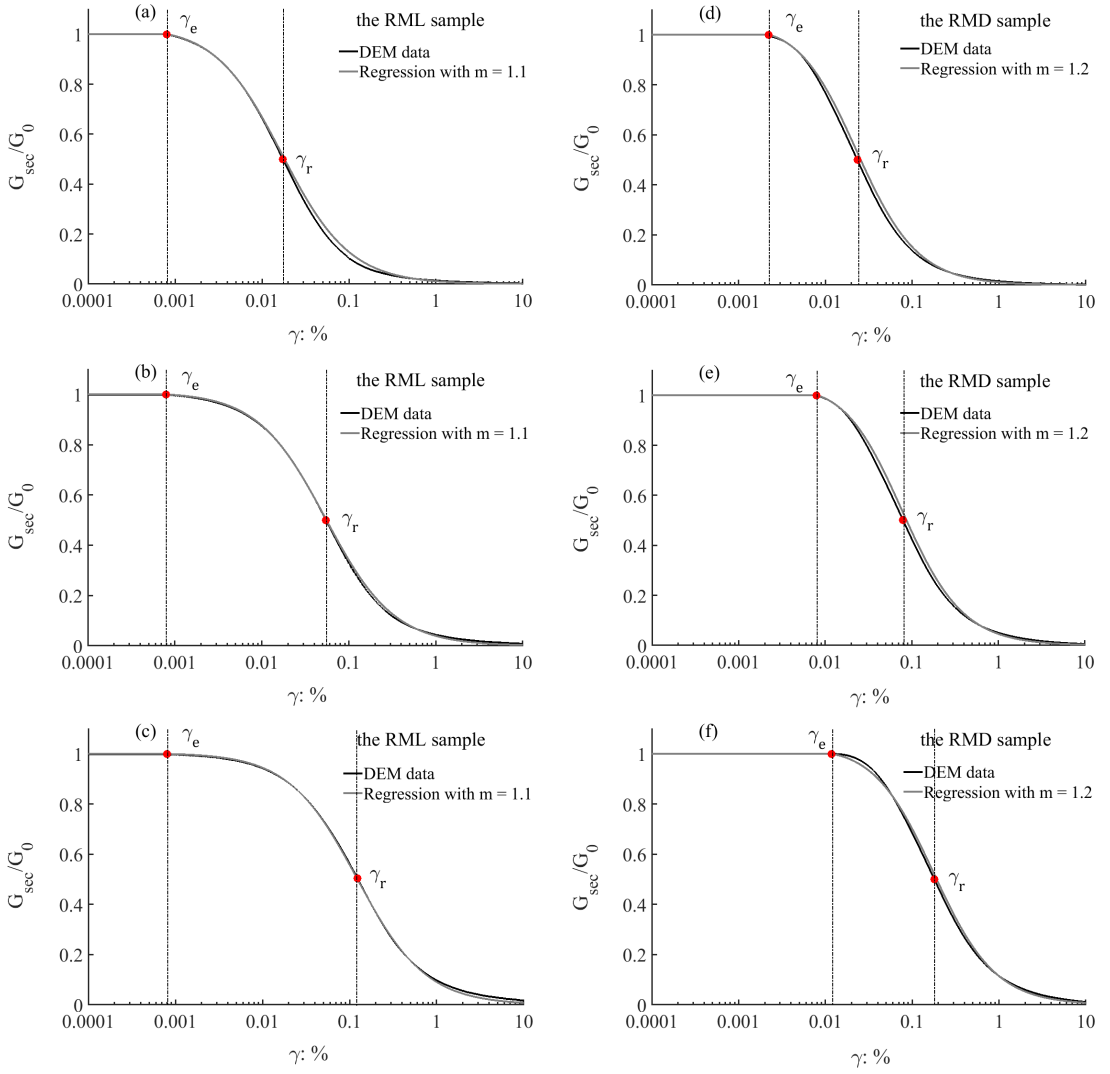

Figure 7: Comparison of hyperbolic equation with DEM data for the dense (RMD) sample and the loose (RML) sample: (a) $p'_0 = 50kPa$: the RML sample; (b) $p'_0 = 300kPa$: the RML sample; and (c) $p'_0 = 1000kPa$: the RML sample; (d) $p'_0 = 50kPa$: the RMD sample; (e) $p'_0 = 300kPa$: the RMD sample; and (f) $p'_0 = 1000kPa$: the RMD sample.

that this micro-scale data is unavailable in the laboratory testing. It is observed from Figure 8 that including N_c in the void ratio correction function seems to be better able to unify the data, particularly for the case of $\gamma < \gamma_e$. First, the adoption of the hyperbolic form of $F(e) = N_c^{\alpha}\frac{(1.186-e)^2}{1+e}$ was conducted to unify the stiffness data. Second, the exponential form of $F(e) = N_c^{\alpha}e^{-\lambda}$ was also considered to remove the effect of the sample density on the stiffness degradation curve. Figure 8 exhibits that cooperation of the micro-scale data into the void ratio correction forms can better unify the shear stiffness.

In addition, analyses of the strain-dependency of $C_p(\gamma)$ and $n(\gamma)$ in the relationship $G_{sec} = C_p(\gamma)F(e)p'^{n(\gamma)}$ were conducted, providing knowledges of non-linear behaviour of granular materials. Oztoprak and Bolton (2013) used

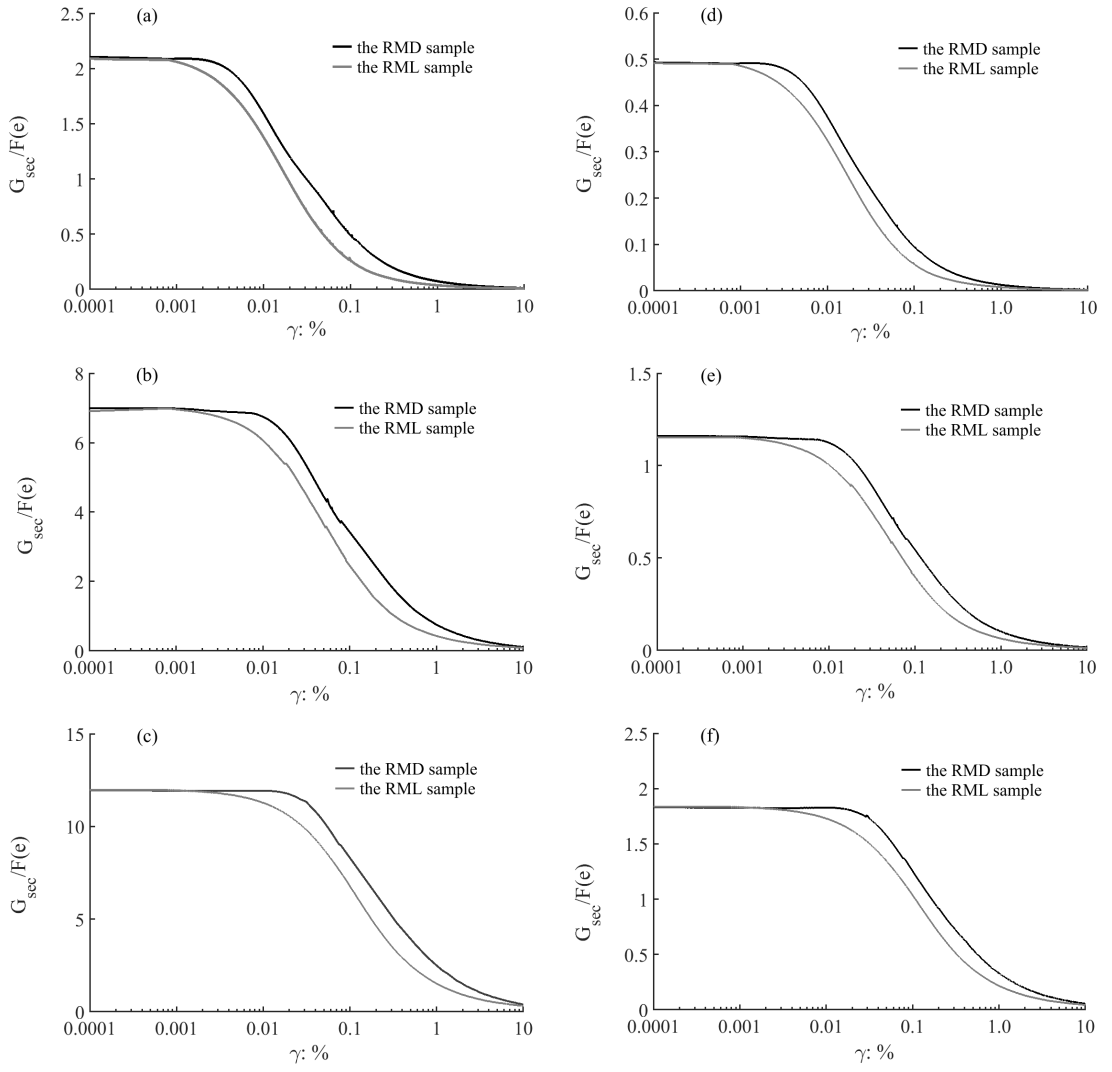

Figure 8: Cooperation the coordination number into both types of void ratio function : (a) $F(e) = N_c^{\alpha}\frac{(1.186-e)^2}{1+e}$, $\alpha = 3.15; p_0' = 50kPa$; (b) $F(e) = N_c^{\alpha}\frac{(1.186-e)^2}{1+e}$, $\alpha = 2.80; p_0' = 300kPa$; (c) $F(e) = N_c^{\alpha}\frac{(1.186-e)^2}{1+e}$, $\alpha = 2.70; p_0' = 1000kPa$; (d) $F(e) = N_c^{\alpha}e^{\lambda}$, $\alpha = 2; \lambda = -3.6; p_0' = 50kPa$; (e) $F(e) = N_c^{\alpha}e^{\lambda}$, $\alpha = 2; \lambda = -3.15; p_0' = 300kPa$; and (f) $F(e) = N_c^{\alpha}e^{\lambda}$, $\alpha = 2; \lambda = -3.0; p_0' = 1000kPa$.

$F(e) = 1/(1+e)^3$ to calculate strain-dependent parameters, $C_p(\gamma)$ and $n(\gamma)$. Plots of $G_{sec}/F(e)p_a'$ against p'/p_a' (i.e. $p_a = 100kPa$) on a log-log scale were used to assess variations in both $C_p(\gamma)$ and $n(\gamma)$ with γ. Denoting $G_{sec}/F(e)p_a'$ as y and naming p'/p_a' as x allows the power relationship $y = C_p x'^n$ to be established, for which both C_p and n are calculated at a given strain level. While $C_p(\gamma)$ reduces with increasing γ, $n(\gamma)$ varies from 0.5 to 1. Using the DEM simulation data, the values of $C_p(\gamma)$ and $n(\gamma)$ are listed in Table 3. Noting that the choice of $F(e)$ has significant effect on both values of $C_p(\gamma)$ and $n(\gamma)$ as previously discussed. In order to calculate the values of C_p and n, the values of G_{sec}, e, N_c, p' were gathered for both samples. Values of $C_p(\gamma)$ and $n(\gamma)$ are calculated by solving the system of

Table 3
Variations in $C_p(\gamma)$ and $n(\gamma)$ with the shear strain for RMD sample being sheared at $p'_0 = 1000kPa$.

	$F(e) = (1+e)^3$		$F(e) = N_c^{\alpha}\frac{(1.186-e)^2}{1+e}$		$F(e) = e^{-\lambda}$	
Strain range	C_p	n	C_p	n	C_p	n
$\gamma = 0.0001\%$	2315.00	0.54	2876.64	0.5452	138.08	0.5463
$\gamma = 0.0002\%$	1133.60	0.87	1411.28	0.8731	121.94	0.0.5937
$\gamma = 0.0003\%$	913.17	0.97	913.17	0.97	1294.29	0.9146
$\gamma = 0.001\%$	859.16	1	1071.06	1	51.24	1
$\gamma = 0.003\%$	830.01	1	1035.13	1	49.50	1
$\gamma = 0.01\%$	786.23	1	985.52	1	46.87	1
$\gamma = 0.03\%$	617.64	1	839.66	1	40.02	1

linear equations such that $\frac{G_{sec}}{F(e)} = log(C_p) + nlog(p')$. The void ratio function $F(e) = N_c^{\alpha}\frac{(1.186-e)^2}{1+e}$ was considered to determine $C_p(\gamma)$ and $n(\gamma)$ with Equation 4.2. Strain-dependent parameters, $C_p(\gamma)$ and $n(\gamma)$ are listed in Table 3, in which the use of $F(e) = N_c^{\alpha}\frac{(1.186-e)^2}{1+e}$ gives identical values of $n(\gamma)$ to those derived from using $F(e) = (1+e)^3$. Numerical values of $C_p(\gamma)$ and $n(\gamma)$ reveal that choice of $F(e)$ partly affect the strain-dependent parameters.

4.3. Evolution of particle interactions during shearing

Evolutions of micro-scale fabric during shearing were analysed, giving more understanding of macro-scale responses of granular materials. Use of a rose diagram was adopted to analyse stress-induced anisotropy on the material fabric. Micro-scale data (i.e. contact number, contact forces and contact stiffness) are assembled within each bin of 10^o using each rose of 180^o. The length of each bin has the information of the magnitude of the number of contacts which are oriented in a range of direction. Particle-scale fabric anisotropy is analysed using three different planes (i.e. xy, xz and yz planes), allowing changes in the stress-induced fabric during shearing to be analysed. A particulate emphasis is placed on the analyses of the stress-induced fabric at three yielding points. Due to fabric isotropy at three yield points, the normal force is almost isotropic for both samples when viewed on the horizontal plane as shown in Figure 9 and Figure 10. Although contact force distributions slightly change at Y_2, the stress-induced fabric becomes remarkably when viewing the degree of stress anisotropy at Y_3 for the RMD samples. The normal force increases significantly in the direction of the principal stress, while a drop in the normal forces is observed for bins with angles varying from 45^o to 135^o. As expected, the patterns of normal force distributions are almost the same for both xz and yz planes. Regarding the evolution of forces at contacts for the RML samples, less anisotropy of material fabric is observed than the RMD samples; however, preferential orientation is observed at Y_3. Moreover, more forces are observed in the directions of the principal stress. These analyses reconfirm that the fabric structure is almost unchanged when samples deform elastically, regardless of the sample density.

Another quantity that can be used to assess changes in material structure is the second-order fabric tensor. This

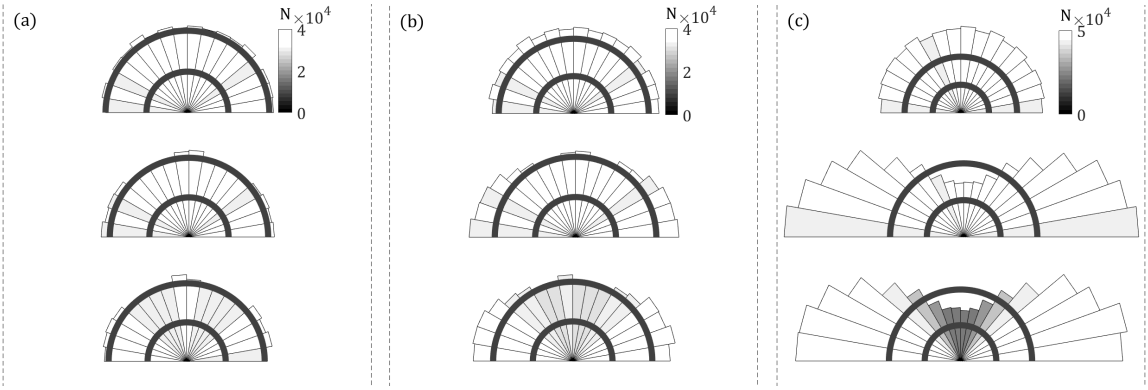

Figure 9: Evolutions of the normal force distributions during shearing, with projections onto the xy, xz and yz planes, respectively for the RMD samples that was sheared at p_0=1000 kPa: (a) Y_1; (b) Y_2; and (c) Y_3.

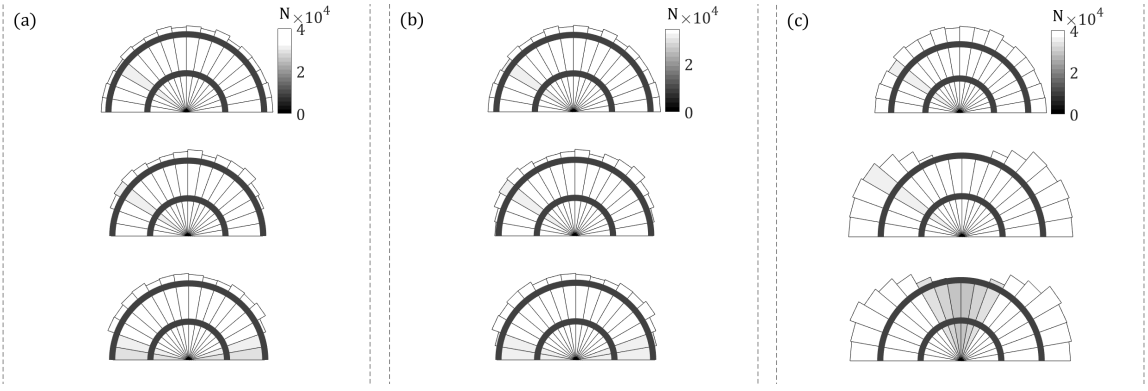

Figure 10: Evolutions of the normal force distributions during shearing, with projections onto the xy, xz and yz planes, respectively for the RML samples that was sheared at p_0=1000 kPa: (a) Y_1; (b) Y_2; and (c) Y_3.

term can be used to determine the dominant orientation of contact distributions in the sample as well as the extent of any bias in the contact orientations. The second-order fabric tensor (Φ_{ij}) is given by the following expression (Satake, 1982):

$$\Phi_{ij} = \frac{1}{N_c} \sum_{c=1}^{c=N_c} n_i^c n_j^c \tag{7}$$

where n_i^c is the contact normal orientation for contact i and N_c is the total number of contacts in the granular assembly.

The ratio of Φ_{xx} with respect to Φ_{zz} may provide a useful quantity to assess changes in anisotropic fabric with the shear deformation. The fabric anisotropy is likely to remain unchanged during the initial stages of shearing. As γ increases, a reduction in Φ_{xx}/Φ_{zz} is observed, revealing a rise in degree of fabric anisotropy due to reorientation of the contacts in both more contact in the $z-$ direction. The nature of the variation in Φ_{xx}/Φ_{zz} with γ is somewhat similar to that of the variation in G_{sec} with γ (see Figure 11). Reduction in Φ_{xx}/Φ_{zz} occurs at a slightly higher strain level. However, reductions in both Φ_{xx}/Φ_{zz} and G_{sec} are observed in zone 2. The changes in contact orientations that

result in measurable variations in the sample fabric were assessed. As the samples were sheared along the stress path in which lateral stress is kept constant and only vertical stress is increased, and so the fabric Φ_{xx}/Φ_{zz} variation is of interest. The fabric is nearly unchanged so long as the behaviour of the system is elastic within zone 1 and zone 2; the ratio Φ_{xx}/Φ_{zz} decreases as the stress state move towards the yield 3 point.

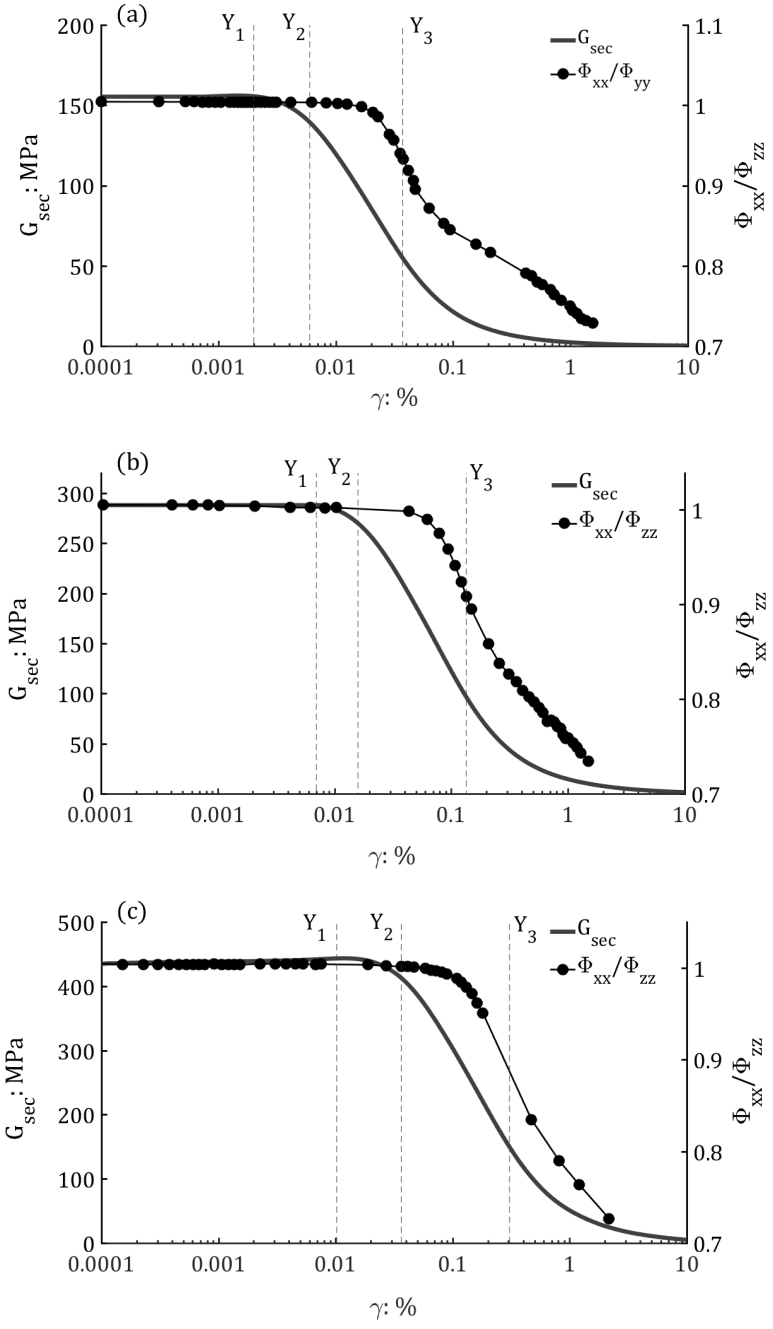

Figure 11: Linking macro-scale yield to the second-order fabric tensor ratio Φ_{xx}/Φ_{zz} for the RMD sample: (a) $p'_0 = 50kPa$; (b) $p'_0 = 300kPa$; and (d) $p'_0 = 1000kPa$

Analyses of normal stiffness are made, giving supplement for changes in stress-induced anisotropy at yield points. It is clear from Figure 12 that normal contact stiffnesses are oriented isotropically on the horizontal plane. However, the degree of anisotropy is observed at Y_3. As expected, the pattern of contact stiffness distribution is identical to that of the force orientations. In contrast, less preferential orientation is exhibited for the RML sample as shown in Figure 13, indicating the density-dependent fabric during shearing.

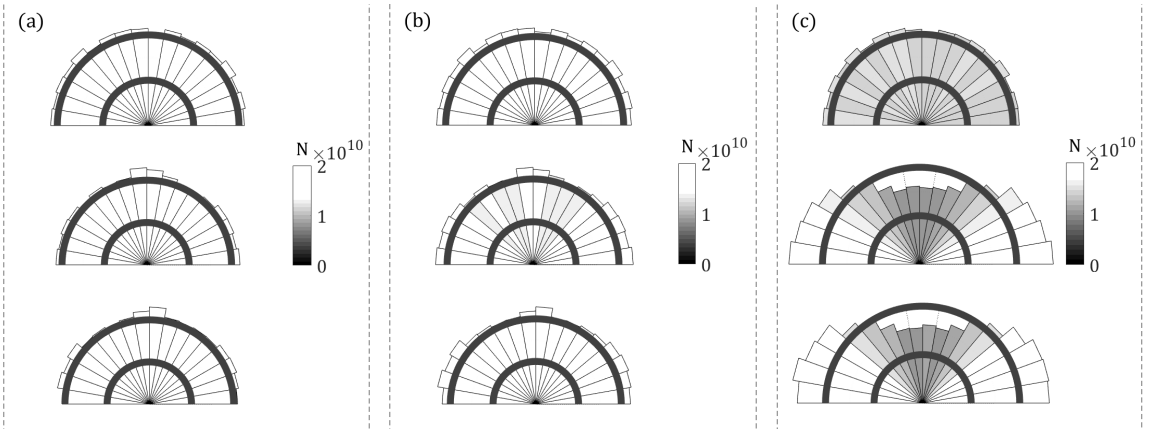

Figure 12: Evolutions of the normal contact stiffness distributions during shearing, with projections onto the xy, xz and yz planes, respectively for the RMD samples that was sheared at p_0=1000 kPa: (a) Y_1; (b) Y_2; and (c) Y_3.

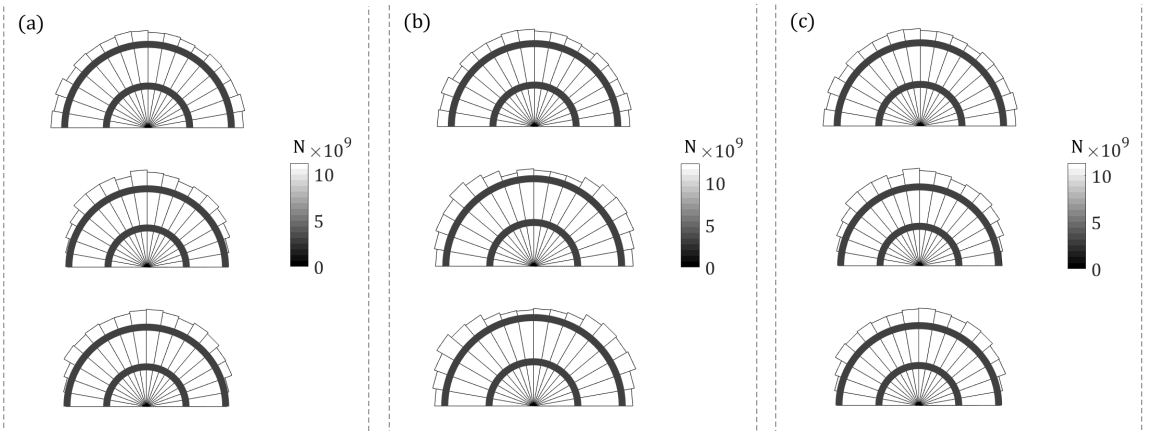

Figure 13: Evolutions of the normal contact stiffness distributions during shearing, with projections onto the xy, xz and yz planes, respectively for the RML samples that was sheared at p_0=1000 kPa: (a) Y_1; (b) Y_2; and (c) Y_3.

It is widely accepted that the link between macro-scale yield and particle scale interactions is dependent upon many factors, the sample density, the stress paths and mean effective stress. Therefore the DEM samples considered had different initial density states. The positions of the yield surfaces were identified from the overall load:deformation behaviour, just as in a laboratory test. The overall sample responses observed in these DEM simulations allow size and positions of the sub-yield surfaces largely depend upon the sample density to be investigated.Evolution of yield surfaces of the RMD sample with the initial confining pressure was shown in Figure 14, reconfirming that sub-yield surfaces

are stress-dependent. In addition, both samples were sheared at an initial confining pressure of $p'_0 = 1000kPa$. The procedure that three yield points are located is the same as that previously described for both samples being sheared along the conventional stress paths. Illustrations of the yield surfaces are shown in Figure 15 where the yield loci are dependent on the stress path. This feature is in excellent agreement with experimental results on sand and clay (Jardine, 1992; Smith et al, 1992; Kuwano and Jardine, 2002).

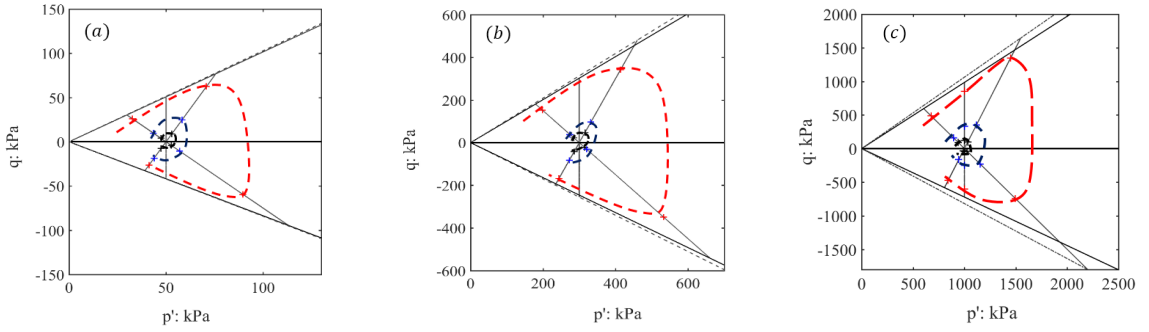

Figure 14: Evolution of yield surfaces of the RMD sample with the initial confining pressure: (a) $p'_0 = 50kPa$; (b) $p'_0 = 300kPa$; and (c) $p'_0 = 1000kPa$.

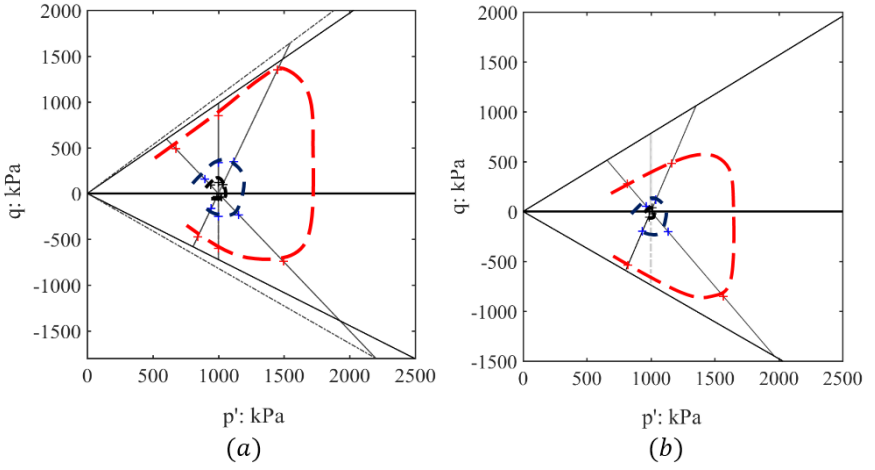

Figure 15: Dependency of sub-yield surfaces on the sample density: (a) RMD samples being sheared at $p'_0 = 1000kPa$; and (b) RML samples being sheared at $p'_0 = 1000kPa$.

4.4. Evolutions of dynamic responses during triaxial shearing

Investigations into evolutions of the shear wave velocities with strain levels were made for both the RMD and RML samples, allowing strain-dependent dynamic stiffness to be explored. Figure 16a shows a comprehensive change in S-wave signals recorded on two rigid walls when the strain level increases, in which the first peaks of the input and output signals tend to reduces when ϵ_a varies from 0.0002% to 0.18%, followed by an expansion of the first peak of

receiving signals. This indicates that the shear wave velocity increases to its peak, after which there is a drop in the magnitude of shear wave velocity. Figure 16b shows changes in the time-domain responses on two rigid walls for the RML samples at different strain levels. Although evolutions of the first-peak responses of S-waves with times are identical to those of the RMD sample, the travel time which is inferred from the first two peaks of signals reduces as the strain level increases. For all cases considered, variations in the cross-correlation signals computed from time-domain responses with time form the same pattern as those of the time-domain responses on two rigid walls. These feature agree very well with experimental work on glass ballotini spheres reported by Otsubo (2016).

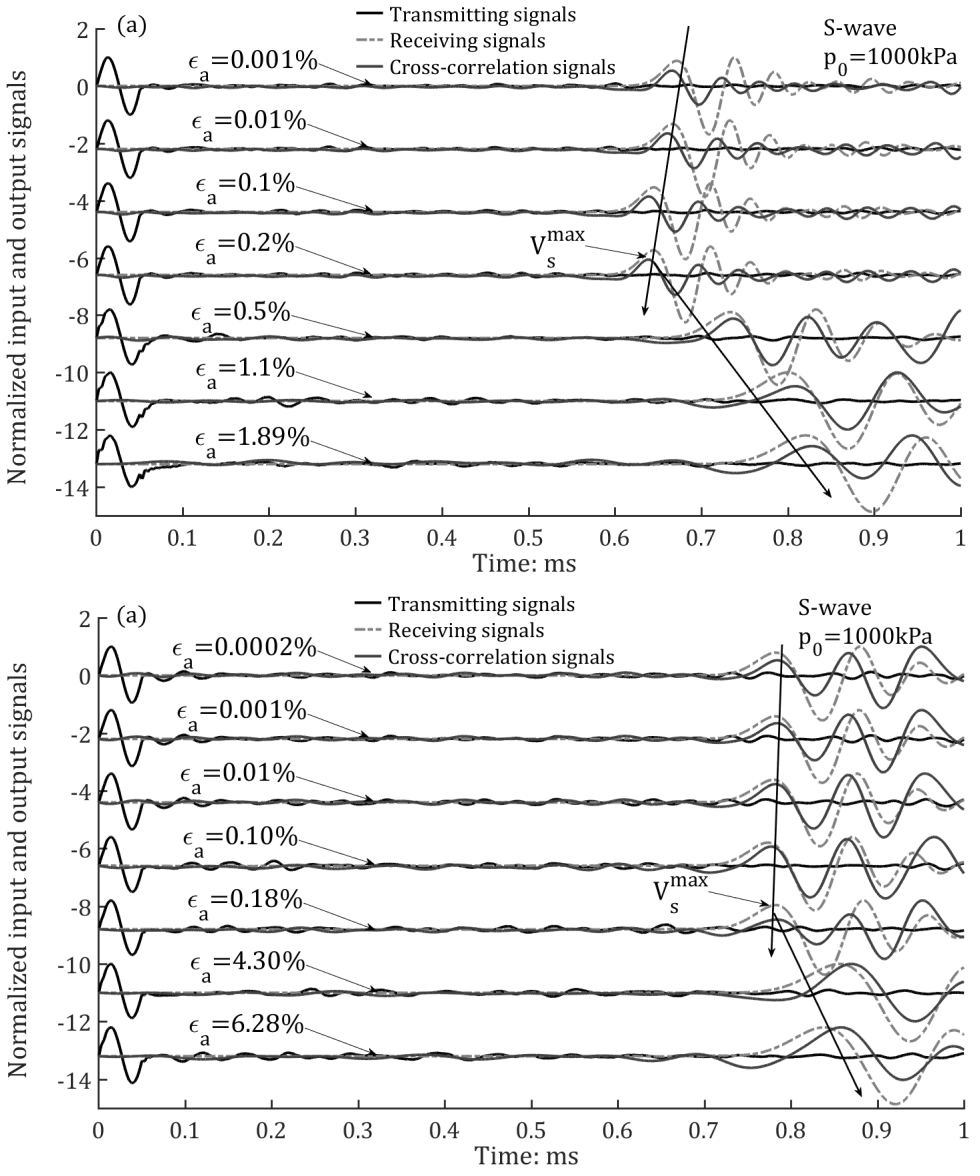

Figure 16: Evolutions of S-wave and P-wave responses for samples that were sheared at p_0=1000kPa: (a) S-wave responses on the rigid walls for the RMD sample; and (b) S-wave responses on the rigid walls for the RML sample.

In addition, analyses of the dependency of the gap between the dynamic stiffness and the static stiffness on the sample density and the initial confining pressure were made using DEM dataset. At each confining stress state, a stress probe of $1kPa$ was used for all samples. These small stress probes aimed at applying very small strain increments so the equivalent stiffness $G_{equ} = \delta q/\delta\epsilon_s$ could be compared with the stiffness from shear wave velocities ($G_{Vs} = \rho_p V_s^2$). The data obtained confirmed that secant stiffness calculated from the stress-strain relationship is almost the same stiffness from dynamic methods for the dense sample as shown in Figure 17. However, observations show that, in contrast to dense specimens, stiffnesses derived from shear wave velocities are about 60% to 70% higher than those from the quasi-static loading for the loose sample. It should be noted that Burland's data (1989) revealed that the stiffness measured by in situ dynamic tests is about 30% higher than those from stress probes at $\epsilon_a = 0.01\%$. Referring to Figure 18 where variations in G_{Vs} with γ is plotted for RML samples. Interestingly, the G_{Vs} is by far higher than G_{sec} as γ increases. Clearly, in the elastic region G_{Vs} remains unchanged while as widely accepted that G_{sec} starts to decay when stress states move to zone 2, implying that gap between G_{Vs} and G_{sec} strongly depends on the sample density when use of the peak-peak method is made to interpret the travel time that shear wave velocity is transmitted through the sample. No evidence is found to explain why there exists the gap; however, motivation in seeking how this gap depends upon the interpretative techniques. This provides some encouragements that various techniques should be adopted to measure G_{Vs}.

It is widely accepted that although the investigation into sensitivity of dynamically measured stiffness to the interpretative method has been the focus of prior research, little attention has been given to the comparison of between statically and dynamically measured stiffness at different strain levels. Three methods which include the time-domain methods, the cross-correlation method and the frequency domain method (O'Donovan, 2013; Nguyen, 2020) are adopted to estimate the shear wave velocities.

4.5. Evolutions of energy dissipation during triaxial shearing

The main purpose here is to observed energy dissipation during shearing for both RMD and RML samples. The question raised is to how energy dissipation evolves within each zone (Jardine, 1992). If, at the contact i, ($f_t^{\beta+\Delta t}$) is equal to or exceeds $\mu_p f_n^{\beta}$, the sliding happens. This results in the dissipation of energy which is calculated as a function of the average tangential force within in a time increment Δt, $(f_t^{\beta+\Delta t} + f_t^{\beta})/2$ where the increment of tangent displacement is $\delta\alpha_t$ as follows:

$$\delta E_f^{\beta} = \frac{f_t^{\beta+\Delta t} + f_t^{\beta}}{2}\delta\alpha_t \tag{8}$$

In DEM simulations, the particle's position and all the force components at each contact are identified in a simple manner, from which the relative increment of tangent displacement, $\delta\alpha_t$ within a chosen timestep, Δt can be determined

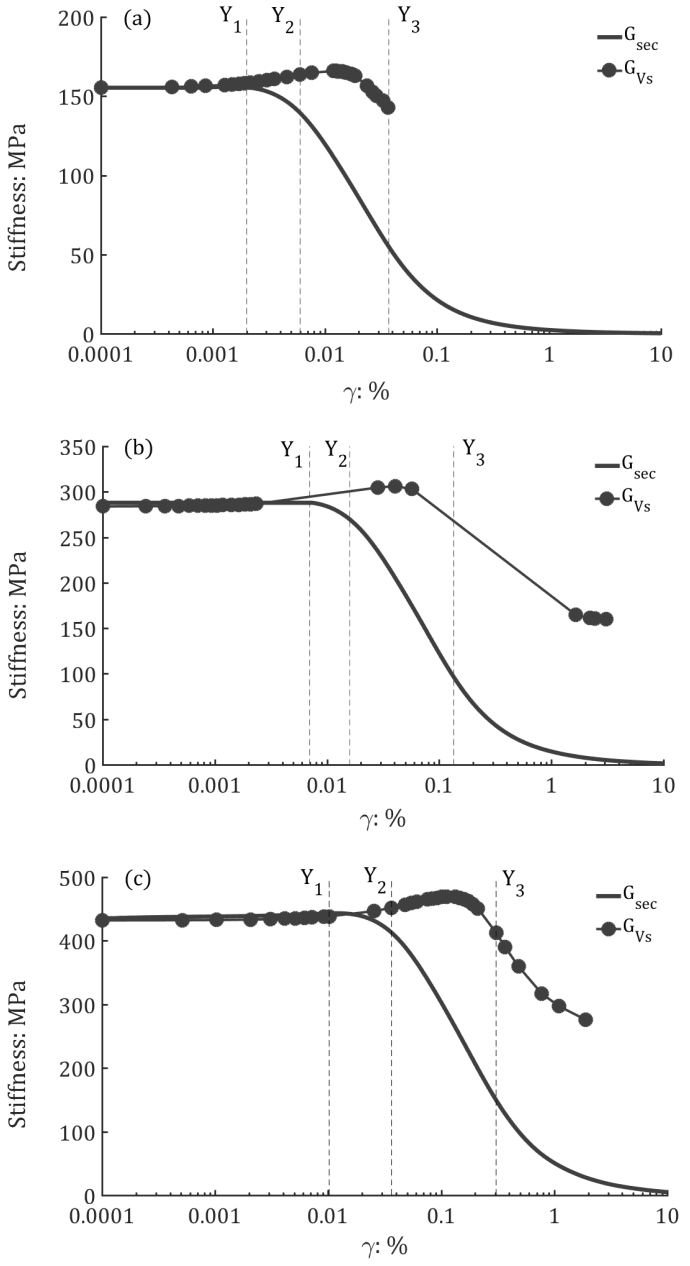

Figure 17: Discrepancies between statically measured stiffness and dynamically measured stiffnesses for RMD samples being sheared at different confining pressures: (a) $p'_0 = 50kPa$; (b) $p'_0 = 300kPa$; and (c) $p'_0 = 1000kPa$.

as $\delta\alpha_t = (f_t^{\beta+\Delta t} - f_t^{\beta})/k_t$. Energy for each time-step must be calculated as the tangent stiffness as the normal force evolves. As stated by Hanley et al. (2018), the frictional dissipation energy is accumulated as

$$\delta E_f^{\beta} = \delta E_f^{\beta-1} + \delta E_f^{\beta} \tag{9}$$

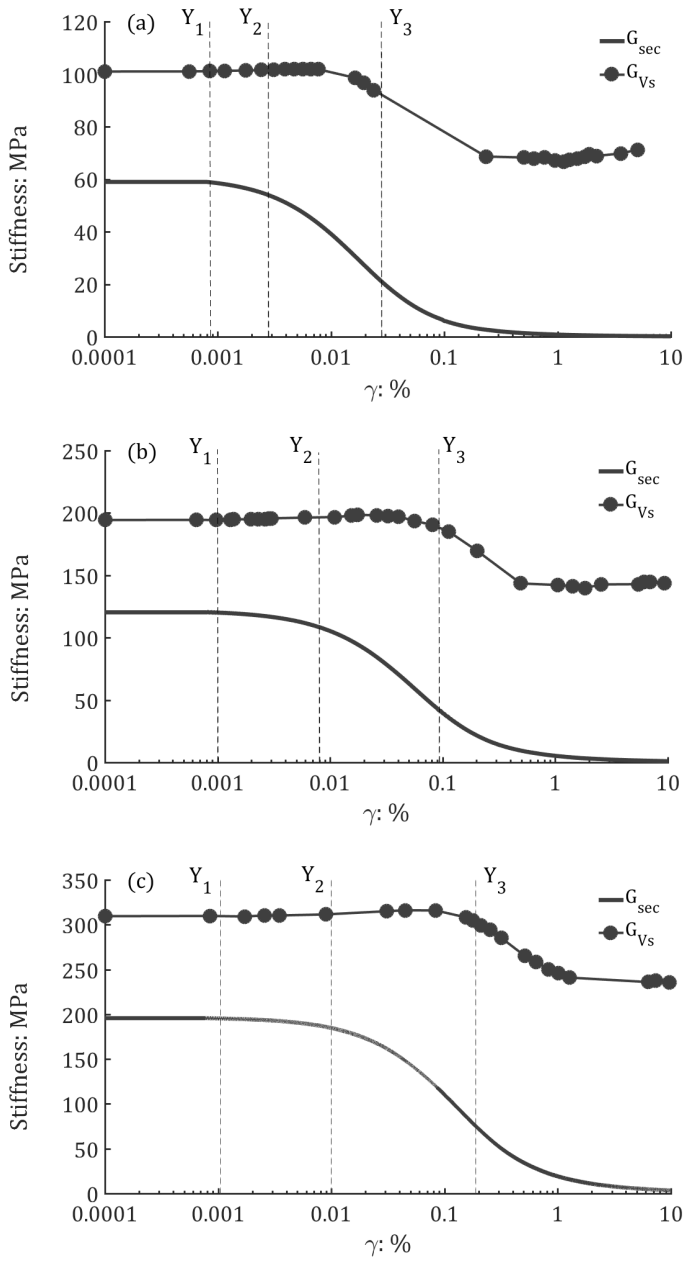

Figure 18: Discrepancies between statically measured stiffness and dynamically measured stiffnesses for RML samples being sheared at different confining pressures: (a) $p'_0 = 50kPa$; (b) $p'_0 = 300kPa$; and (c) $p'_0 = 1000kPa$.

A process to calculate this energy is implemented in the LAMMPS code used here. Hanley et al. (2018) stated that the boundary work input and the friction energy dissipated are almost equal during triaxial shearing. This means that much of the work input transfers into dissipated energy through sliding at the contacts. This finding agrees well with the assumption of Schofield and Wroth (1968) that plastic work is dissipated by sliding. The energy associated with the normal force is the normal component of strain energy; the energy related to a relative increment of tangent

displacement is called the tangential component of strain energy.

The normal force, F_n and the normal overlap, α_n give the normal strain energy that can be calculated as follows:

$$E_{sn} = \int_0^{\alpha_n} F_n d\alpha_n = \int_0^{\alpha_n} \frac{4G_p r_e}{3(1-\nu_p)} \delta_n^{\frac{3}{2}} n d\alpha_n = \frac{2}{5}|F_n|\alpha_n \tag{10}$$

A strain energy component arises from the tangential force that does not cause sliding occurred at the contact (i.e. $F_t < F_n/\mu_{pp}$) and if the relative increment of tangent displacement at the contact for one time-step is α_t, the tangential strain energy can be calculated as follows:

$$E_{st} = F_t \alpha_t = \frac{f_t^{\beta+\Delta t} + f_t^{\beta}}{2} \alpha_t = \left| \frac{f_t^{\beta+\Delta t} + f_t^{\beta}}{2} \right| \left| \frac{f_t^{\beta+\Delta t} - f_t^{\beta}}{k_t} \right| \tag{11}$$

Hanley et al. (2018) showed that the shear strain energy is two orders of magnitude lower than the normal strain energy. An assessment of the error in the energy balance was first made to provide a check on the numerical stability as noted as O'Sullivan (2011b) and Hanley et al. (2018). Analysis of the error for the RMD sample that was sheared at $p_0' = 1000kPa$ is shown in Figure 19 where the magnitude of such error in energy balance which was divided by boundary work is relatively small (almost zero) at large-scale levels, confirming that the stability of all simulations is satisfied.

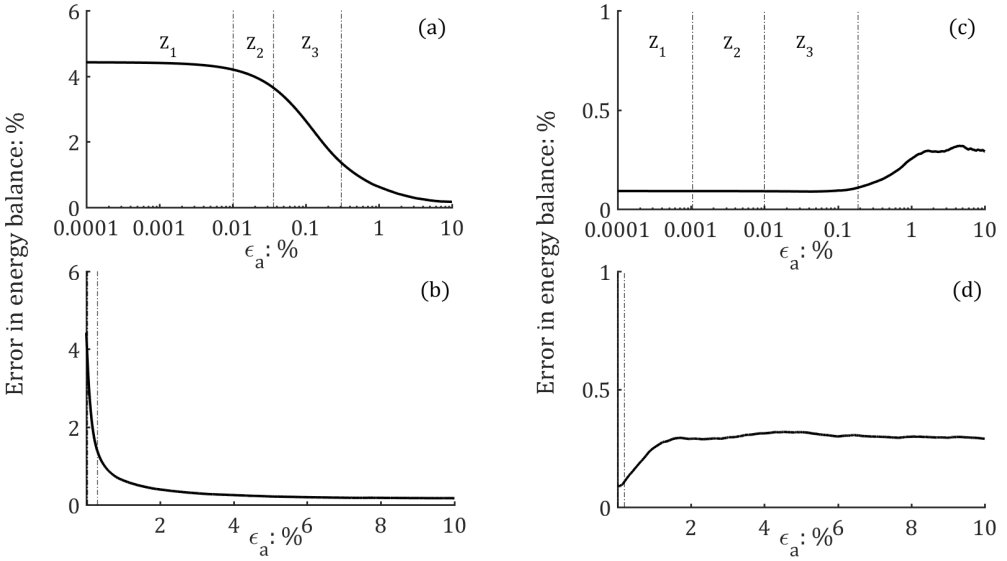

Figure 19: Error in the energy balance expressed as a percentage of the boundary work against axial strain (%) for the samples that were sheared at $p_0' = 1000kPa$: (a) the RMD sample: linear scale; (b) the RMD sample: logarithm scale; (c) the RML sample: linear scale; and (d) the RML sample: logarithm scale.

Hanley et al. (2018) analysed the evolution of energy during shearing, with a focus on the comparison of energy dissipation due to sliding with the boundary work. Their DEM data confirmed that both energies are almost equal. To

further understanding how the boundary work is dissipated through particle movement and rearrangement and due to sliding at the contacts, these individual energy components are analyzed within each of the zones proposed by Jardine (1992). Noting that the terms Z_1, Z_2 and Z_3 are denoted as zone 1, zone 2 and zone 3, respectively. Figure 20a confirms that friction and boundary work, B_w are almost the same for the RMD samples; however, a gap appears when stress states are within zone 3. The normal component of the strain energy stored at the contacts shown in Figure 20c can explain this gap between the frictional dissipation and boundary work. The boundary work can be decomposed into the volumetric work (i.e. V_w) and the distortional work (i.e. W_d), and the evolution of these energies are plotted in Figure 20b where different trends for such energies are observed, most probably due to shrinkage of the sample volume while there is an increasing in the shear strain. Figure 20d shows that kinematic energies are almost zeros within zone 1 and zone 2, with a slight evolution in the material structure.

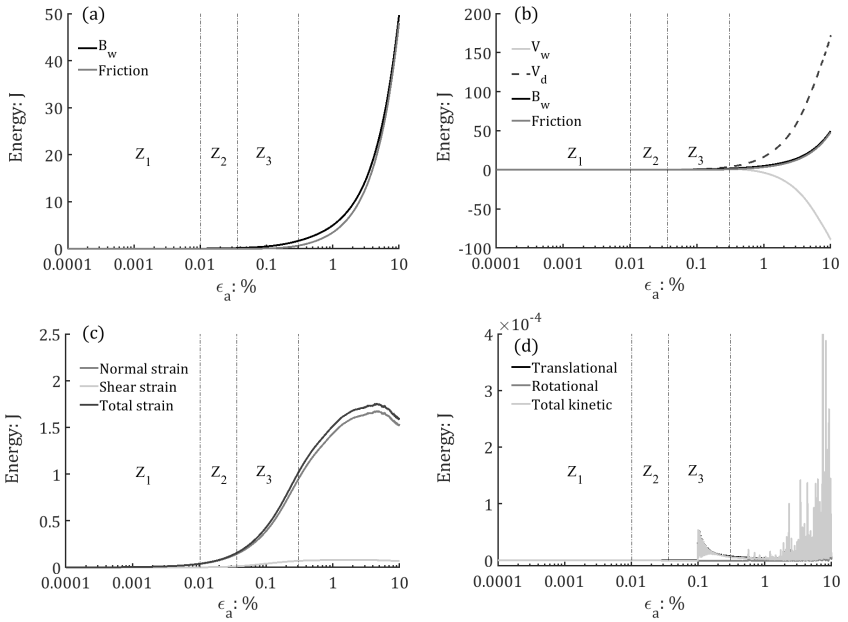

Figure 20: Macro-scale and micro-scale energy during shearing for the RMD sample that was sheared at $p'_0 = 1000kPa$ (a) friction and boundary work; (b) volumetric and distortional work; (c) strain energy; and (d) kinetic energy.

The evolution of each energy component for the RML sample was shown in Figure 21 where a smaller gap between the boundary work and friction is observed, most probably due to the smaller strain energy stored at the contacts in comparison with the RMD case. Although all the energy components follow the same trend as for the RMD sample, the magnitude of each energy component is slightly smaller for the RML sample. As expected, the translational energy is slightly higher than that of the RMD sample; however, less energy is required for volumetric deformation because of the dilatancy.

The variation in the patterns of energy dissipation in the RMD samples in energy components with confining

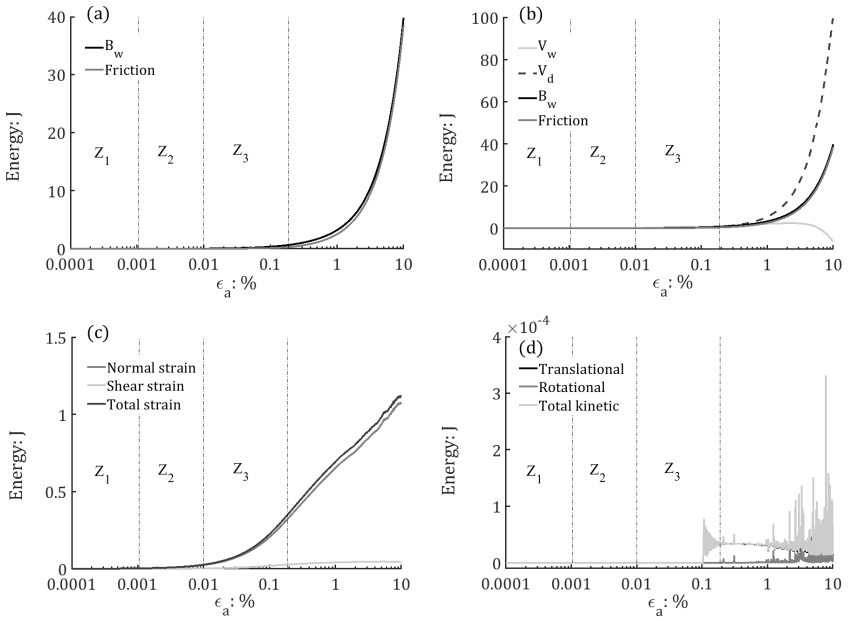

Figure 21: Macro-scale and micro-scale energy of the compression triaxial test for the RML sample that was sheared at $p'_0 = 1000kPa$ (a) friction and boundary work; (b) volumetric and distortional work; (c) strain energy; and (d) kinetic energy.

pressure is shown in Figure 22, indicating the density-dependent and stress-dependent volumetric and distortional work. Moreover, the strain energy depends on the confining pressure but its variation is relatively small, confirming that almost the boundary work is transferred into the friction. Allied to tracing energy component for the RMD sample, analyses of the evolution of the energy components were made for the RML sample. Figure 23 exhibits that the energy component of the RML sample has the same pattern as those of the RMD sample.

4.6. Effect of particle size distribution on the degradation of stiffness with increasing strain

Figure 24a shows reductions in E_{sec} and G_{sec} for the samples with $C_u = 2$ and $C_u = 3$. Numerical results show that the sample with the higher value of C_u has a smaller magnitude of E_{sec}. Values of both E_{sec} and G_{sec} at small-strain levels show the relationship of $E_{sec} = 2(1 + \nu)G_{sec}$, with $\nu < 0.5$. Figure 25a shows degradations of E_{sec} and G_{sec} with the shear strain for the sample with $C_u = 2$. Two values of interparticle friction, i.e. $\mu_p = 0.2$ and $\mu_p = 0.3$ were used in the isotropic compression phase, in which the samples were loaded to a mean effective confining pressure of $p'_0 = 1000kPa$. Numerical results reveal that the sample with a higher value of the interparticle friction has a lower value of shear stiffness. In addition, it is observed from Figure 25b that as C_u increases, both E_{sec} and G_{sec} reduce.

In addition, an appraisal of the influence of interparticle friction on the shear stiffness was made by adopting three different values of μ_p in order to generate samples with different densities. Three values were adopted in the isotropic

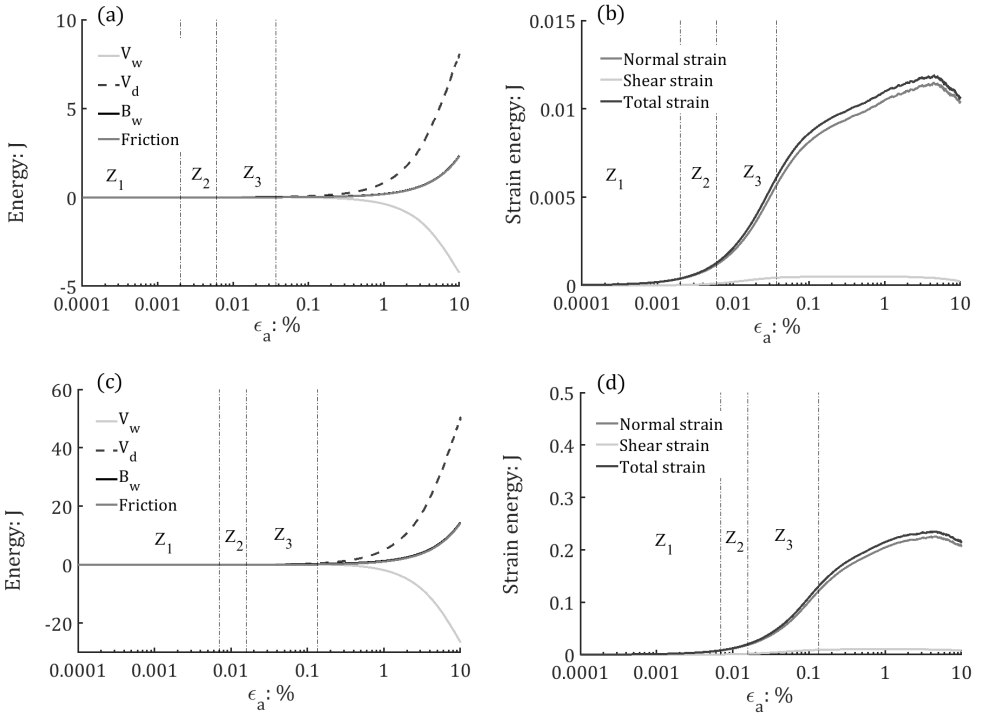

Figure 22: Evolution of energy components for the RMD sample: (a) $p'_0 = 50kPa$: friction, boundary work, volumetric and distortional work; (c) $p'_0 = 50kPa$: strain energy; (c) $p'_0 = 300kPa$: friction, boundary work, volumetric and distortional work; and (d) $p'_0 = 300kPa$: strain energy.

compression to an isotropic mean effective of pressure $p_0 = 1000kPa$. It is shown in Figure 26 that samples with the use of higher values of μ_p have lower the shear modulus.

Figure 27 shows the stiffness degradation curve for the samples with $C_u = 5$ and $C_u = 6$. Interestingly, the shape of the two samples is almost identical, indicating that increases in the C_u for this linear-graded samples PSD might does not affect the non-linear stiffness-strain relationship when C_u increases beyond a certain value.

Although the overall response and energy dissipations during shearing depend upon the values of C_u, these issues have received little attention. Figure 28 shows how the energy dissipation evolves with the shear strain and the dependency of energy dissipations of the sample on C_u. DEM results show that the sample with a lower value of C_u has a higher energy dissipation. As expected, when the value of C_u increases, the amount of the energy dissipation and the strain energy stored at the contacts reduce, most probably likely that there is little sliding associated with the finer particles. The gap between the work input and the frictional energy tends to reduce as C_u increases due to the smaller amount of energy stored at the contact. Moreover, for the cases of $C_u = 2$ and $C_u = 3$ energy dissipated through sliding at contacts is almost identical; however, slight drops in both components of strain energy are exhibited. For samples with $C_u = 5$ and $C_u = 6$, the friction and the input work are almost equal, along with the same amount of strain energy as shown in Figure 28c and 28d.

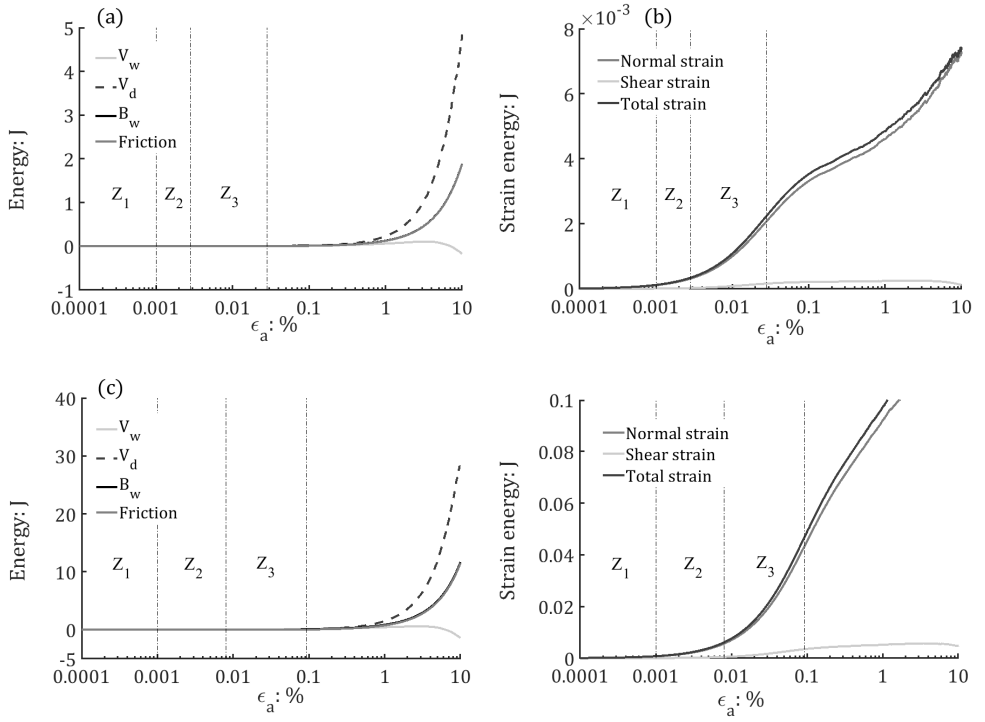

Figure 23: Evolution of energy components for the RML sample: (a) $p'_0 = 50kPa$: friction, boundary work, volumetric and distortional work; (c) $p'_0 = 50kPa$: strain energy; (c) $p'_0 = 300kPa$: friction, boundary work, volumetric and distortional work; and (d) $p'_0 = 300kPa$: strain energy.

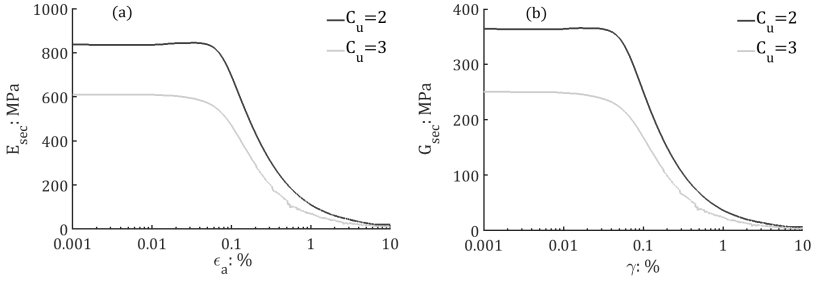

Figure 24: Effect of C_u on the stiffness degradation curve, i.e. the variation in stiffness with shear strain, for loose samples with $C_u = 2$ and $C_u = 3$: (a) E_{sec} ; and (b) G_{sec}.

The curvature number was calculated for samples with various values of C_u and then checked against the formulation introduced by Oztoprak and Bolton (2013). Numerical results were reported in Table 4 where m decreases as C_u increases, agreeing very well with the Equation proposed by Oztoprak and Bolton (2013). However, the DEM dataset gives a slightly higher value of m. Interestingly, when C_u increases to a limiting value, the value of m is likely to be unchanged. This provides support for the almost identical stiffness degradation curves for the samples with $C_u = 5$ and $C_u = 6$ as shown in Figure 27.

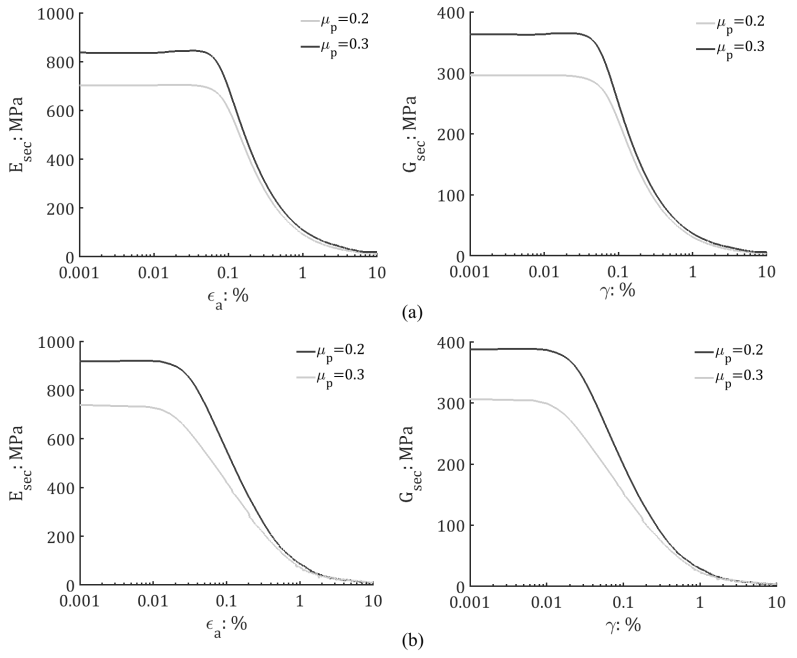

Figure 25: Effect of C_u on the stiffness degradation curve for samples that was sheared at $p'_0 = 1000kPa$: (a) E_{sec} and G_{sec} for the samples with $C_u = 2$; and (b) E_{sec} and G_{sec} for the samples with $C_u = 3$.

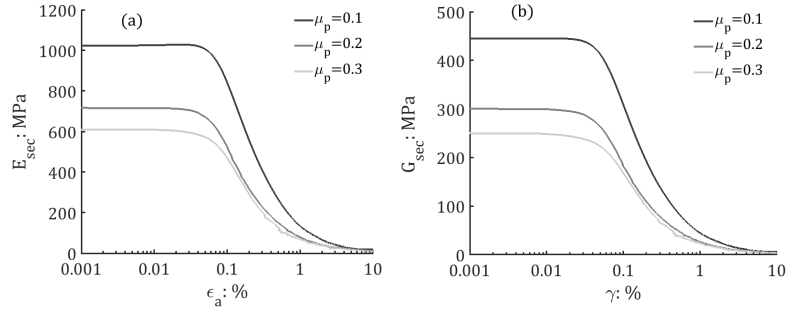

Figure 26: Effect of μ_p on the stiffness degradation curve for the loose, medium and dense samples with $C_u = 3$ that were sheared at $p'_0 = 1000kPa$.

5. Conclusion

The DEM simulations can model the highly complex behaviour of granular materials, allowing strain-dependent stiffness and stress-dependent stiffness to be studied. The use of hyperbolic expressions allows an S: shape of the stiffness degradation curve to be captured well. With a few parameters in the expressions, the nonlinearity of stiffness in granular materials can be modelled. Numerical results reveal that the inclusions of micro-scale data (i.e. the coordination number) is likely to give a more accurate void ratio correction function when compared with the traditional function used in the interpretation of laboratory test data where particle level information is unavailable. Values of $C_p(\gamma)$ and $n(\gamma)$ in $G_{sec} = C_p(\gamma)F(e)p'^{n(\gamma)}$ are calculated for various ranges of strain level, producing the fundamental

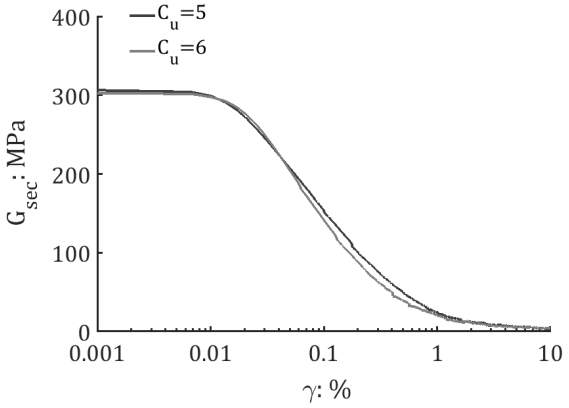

Figure 27: The stiffness degradation curve for the loose samples with $C_u = 5$ and $C_u = 6$ sheared at $p'_0 = 1000kPa$.

Table 4
Dependency of the curvature parameter, m on the samples with various values of C_u.

C_u	$m = C_u^{-0.075}$	m approximated from DEM data
$C_u = 2$	0.9493	1.35
$C_u = 3$	0.9209	1.30
$C_u = 5$	0.8863	1.05
$C_u = 6$	0.8743	1.05

knowledge of the non-linear stiffness of granular media. In addition, the inclusions of micro-scale data (i.e. the coordination number) will likely give a more accurate void ratio correction function when compared with the traditional function used in the interpretation of laboratory test data where particle level information is unavailable."

Using the peak-peak method, both methods render almost the same values of stiffness when granular behaviour is elastic (within zone 2); however, the dynamically measured stiffness is far larger than the statically measured stiffness for the loose sample. The magnitude of the dynamic stiffness remains almost unchanged in zone 1, followed by a steady increase to its peaks that occurs in zone 3 before experience of a drop in its magnitude. This is in contrast to the trend that the statically measured stiffness is almost constant in zone 1 and then drops steadily when strain levels increase. Evolution of the coordination number with increasing strain levels is attributable for the trend that the dynamic stiffness varies as the shear strain increases. Another striking feature is that the constrained modulus measured from the compression wave velocity continues to increase with increasing strain levels for the loose sample; however, the variation in the constrained modulus with strain level has the same trend as that of the shear modulus for the dense sample. In addition, the discrepancy between the shear stiffness determined using both methods is likely to be less dependent on the stress level. However, these gaps become slightly smaller at lower confining stress. Changes in the input frequency make very small alterations in the magnitude of dynamic stiffness. Discrepancies between statically and dynamically measured stiffness depend largely on the sample's density. Moreover, It was observed that

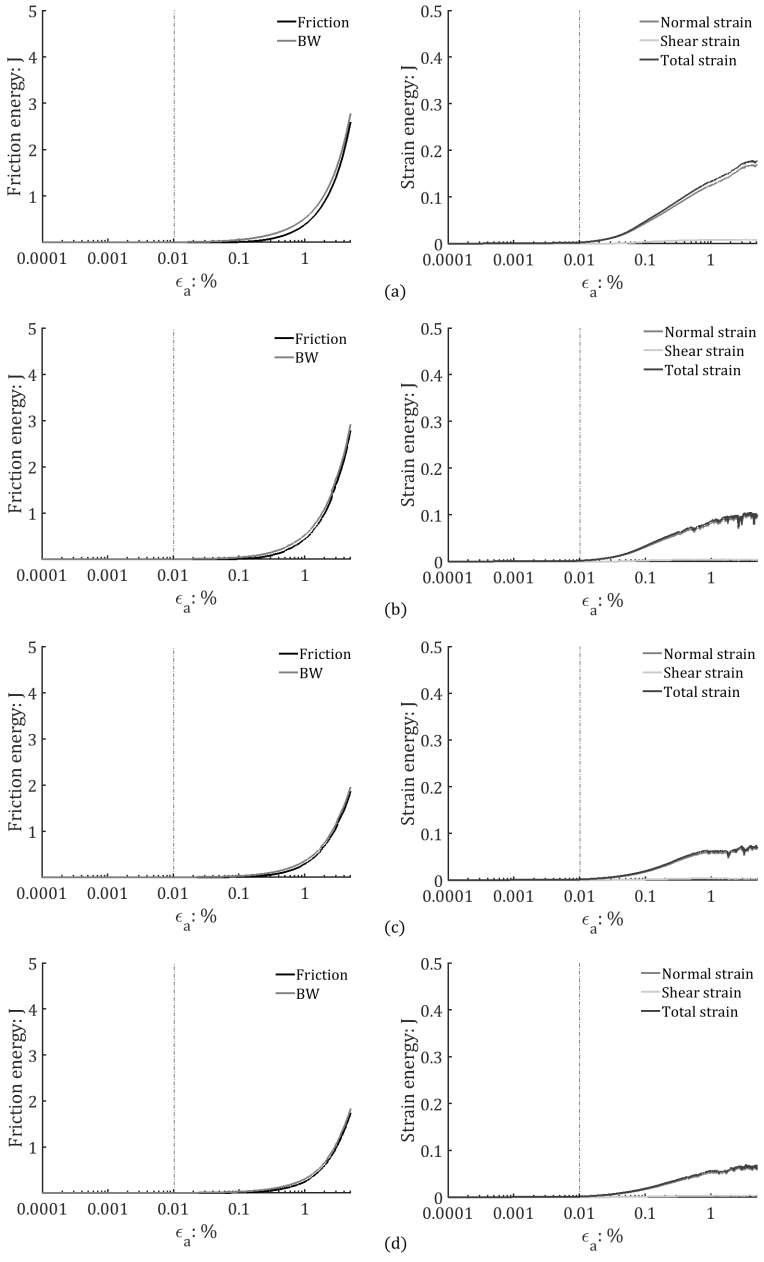

Figure 28: Dependency of friction and strain energy on the PSDs using $\mu_p = 0.30$ during shearing: (a) $C_u = 2$; (b) $C_u = 3$; (c) $C_u = 5$; and (d) $C_u = 6$.

variations in dynamically measured stiffness follow the same trend as changes in the coordination number as the shear strain increases. It is reasonable to conclude that shear wave velocities depend on the average contact per particle. The variation in the ratio Φ_{xx}/Φ_{zz} also follows a similar trend to the variation in dynamically measured stiffness with shear strain.

Several DEM simulations that consider effects of the coefficient of uniformity (C_u) on the non-linear behaviour of

granular materials are performed, arriving at some key observations that: (i) samples with lower values of C_u have higher stiffness at small-strain levels; (ii) a higher amount of work should be input for samples with coarse particles to attain a particular strain level; (iii) more energy dissipation is observed for samples with a lower C_u value.

6. Acknowledgements

This is part of the TPS project. All simulations were conducted using a modified version of the open-source code, Granular LAMMPS developed at Imperial College London. The author is grateful to the DEM group at Imperial College led by Prof. Catherine O'Sullivan for allowing the author to pursue the topic in which the author is interested. Special thanks must go to Dr Kevin Hanley and Dr Thomas Shire for their enormous contributions to the modified version of LAMMPS granular code and for the MATLAB script for the coefficient of uniformity. He is also grateful to a Vied-Newton PhD scholarship and a Dixon scholarship from Imperial College London, UK, for supporting his studies at Imperial College London. He is also indebted to the Dean's Fund from Imperial College London for financial support (2020, 2019, 2018, 2017).

References

Adesina, P., O'Sullivan, C., Morimoto, T., Otsubo, M., 2022. Determining a representative element volume for DEM simulations of samples with non-circular particles. Particuology, 68, 29-43.

Atkinson, J.H., 2000. Non-linear soil stiffness in routine design. Géotechnique, 50(5), pp.487-508.

Atkinson, J.H., Richardson, D. and Stallebrass, S.E., 1990. Effect of recent stress history on the stiffness of overconsolidated soil. Géotechnique, 40(4), pp.531-540.

Bellotti, R., Jamiolkowski, M., Presti, D. L., and O'neill, D.A., 1996. Anisotropy of small strain stiffness in Ticino sand. Geotechnique, 46(1), 115-131.

Bolton, M.D., Nakata, Y. and Cheng, Y.P., 2008. Micro-and macro-mechanical behaviour of DEM crushable materials. Géotechnique, 58(6), pp.471-480.

Cho, G.C., Dodds, J. and Santamarina, J.C., 2007. Closure to "Particle Shape Effects on Packing Density, Stiffness, and Strength: Natural and Crushed Sands" by Gye-Chun Cho, Jake Dodds, and J. Carlos Santamarina. Journal of geotechnical and geoenvironmental engineering, 133(11), pp.1474-1474.

Ciantia, M.O., Arroyo, M., O'Sullivan, C., Gens, A., Liu, T., 2019. Grading evolution and critical state in a discrete numerical model of Fontainebleau sand. Géotechnique, 69(1), 1-15.

Clayton, C.R.I., 2011. Stiffness at small strain: research and practice. Géotechnique, 61(1), pp.5-37.

Cundall, P.A. and Strack, O.D., 1979. A discrete numerical model for granular assemblies. geotechnique, 29(1), pp.47-65.

Darendeli, M.B., 2001. Development of a new family of normalized modulus reduction and material damping curves. The university of Texas at Austin.

Fahey, M. and Carter, J.P., 1993. A finite element study of the pressuremeter test in sand using a nonlinear elastic plastic model. Canadian Geotechnical Journal, 30(2), pp.348-362.

Greening, P.D., and Nash, D.F., 2004. Frequency domain determination of G_0 using bender elements. Geotechnical testing journal, 27(3), 288-294.

Hanley, K.J., Huang, X. and O'Sullivan, C., 2018. Energy dissipation in soil samples during drained triaxial shearing. Géotechnique, 68(5), pp.421-433.

Hardin, B.O. and Drnevich, V.P., 1972. Shear modulus and damping in soils: design equations and curves. Journal of the Soil mechanics and Foundations Division, 98(7), pp.667-692.

Huang, X., Hanley, K.J., O'Sullivan, C., Kwok, F.C., 2014. Effect of sample size on the response of DEM samples with a realistic grading. Particuology, 15, 107-115.

Houlsby, G.T. and Wroth, C.P., 1991. The variation of shear modulus of a clay with pressure and overconsolidation ratio. Soils and Foundations, 31(3), pp.138-143.

Houlsby, G.T., 2009. Potential particles: a method for modelling non-circular particles in DEM. Computers and Geotechnics, 36(6), 953-959.

Jardine, R.J., Symes, M.J. and Burland, J.B., 1984. The measurement of soil stiffness in the triaxial apparatus. Geotechnique, 34(3), pp.323-340.

Jardine, R.J., Potts, D.M., Fourie, A.B. and Burland, J.B., 1986. Studies of the influence of non-linear stress–strain characteristics in soil–structure interaction. Geotechnique, 36(3), pp.377-396.

Jardine, R.J., 1992. Some observations on the kinematic nature of soil stiffness. Soils and foundations, 32(2), pp.111-124.

Jovičić, V., and Coop, M.P., 1998. The measurement of stiffness anisotropy in clays with bender element tests in the triaxial apparatus. Geotechnical Testing Journal, 21(1), 3-10.

Kuwano, R. and Jardine, R.J., 2002. On the applicability of cross-anisotropic elasticity to granular materials at very small strains. Géotechnique, 52(10), pp.727-749.

Liu, D., O'Sullivan, C. and Carraro, J.A.H., 2021. Influence of Particle Size Distribution on the Proportion of Stress-Transmitting Particles and Implications for Measures of Soil State. Journal of Geotechnical and Geoenvironmental Engineering, 147(3), p.04020182.

Liu, X. and Yang, J., 2018. Shear wave velocity in sand: effect of grain shape. Géotechnique, 68(8), pp.742-748.

Liu, X., Yang, J., Wang, G. and Chen, L., 2016. Small-strain shear modulus of volcanic granular soil: An experimental investigation. Soil Dynamics and Earthquake Engineering, 86, pp.15-24.

Menq, F.Y., 2003. Dynamic properties of sandy and gravelly soils (Doctoral dissertation).

Nguyen, H., Otsubo, M. and O'Sullivan, C., 2017. An appraisal of the influence of material fabric and stress anisotropy on small-strain stiffness. In EPJ web of conferences (Vol. 140, p. 12005). EDP Sciences.

Nguyen, H.C., O'Sullivan, C. and Otsubo, M., 2018. Discrete element method analysis of small-strain stiffness under anisotropic stress states. Géotechnique Letters, 8(3), pp.183-189.

Nguyen, H. and O'Sullivan, C., 2019. Linking macro-scale yielding and micro-scale response. In E3S Web of Conferences (Vol. 92, p. 14008). EDP Sciences.

Nguyen, H., 2020. Micromechanics of shear wave propagation and non-linear stiffness of granular materials (Doctoral dissertation, Imperial College London).

Nguyen, H.C., 2021. Evolution of the coefficient of lateral earth pressure at rest with interparticle friction: a numerical study. In EPJ Web of Conferences (Vol. 249, p. 08015). EDP Sciences.

O'Donovan, J., 2013. Micromechanics of wave propagation through granular material (Doctoral dissertation, Imperial College London).

O'Sullivan, C., 2011. Particle-based discrete element modeling: geomechanics perspective. International Journal of Geomechanics, 11(6), pp.449-464.

O'Sullivan, C., 2011. Particulate discrete element modelling: a geomechanics perspective. CRC Press.

Otsubo, M., 2016. Particle scale analysis of soil stiffness and elastic wave propagation (Doctoral dissertation, Imperial College London).

Otsubo, M., O'Sullivan, C. and Shire, T., 2017. Empirical assessment of the critical time increment in explicit particulate discrete element method simulations. Computers and Geotechnics, 86, pp.67-79.

Oztoprak, S. and Bolton, M.D., 2013. Stiffness of sands through a laboratory test database. Géotechnique, 63(1), pp.54-70.

Plimpton, S., 1995. Fast parallel algorithms for short-range molecular dynamics. Journal of computational physics, 117(1), pp.1-19.

Schofield, A. and Wroth, P., 1968. Critical state soil mechanics. McGraw-hill.

Shire, T., 2014. Micro-scale modelling of granular filters (Doctoral dissertation, Imperial College London).

Shire, T. and O'Sullivan, C., 2016. Constriction size distributions of granular filters: a numerical study. Géotechnique, 66(10), pp.826-839.

Smith, P.R., Jardine, R.J. and Hight, D.W., 1992. The yielding of Bothkennar clay. Géotechnique, 42(2), pp.257-274.

Thornton, C. and Antony, S.J., 1998. Quasi–static deformation of particulate media. Philosophical Transactions of the Royal Society of London. Series A: Mathematical, Physical and Engineering Sciences, 356(1747), pp.2763-2782.

Viggiani, G. and Atkinson, J.H. 1995. Interpretation of bender element tests. Geotechnique, 45(1), 149-154.

Wichtmann, T. and Triantafyllidis, T., 2009. Influence of the grain-size distribution curve of quartz sand on the small strain shear modulus G max. Journal of geotechnical and geoenvironmental engineering, 135(10), pp.1404-1418.

Xiao, Y., Stuedlein, A.W., Ran, J., Evans, T.M., Cheng, L., Liu, H., Van Paassen, L.A. and Chu, J., 2019. Effect of particle shape on strength and stiffness of biocemented glass beads. Journal of Geotechnical and Geoenvironmental Engineering, 145(11), p.06019016.